CHALMERS
UNIVERSITY OF TECHNOLOGY

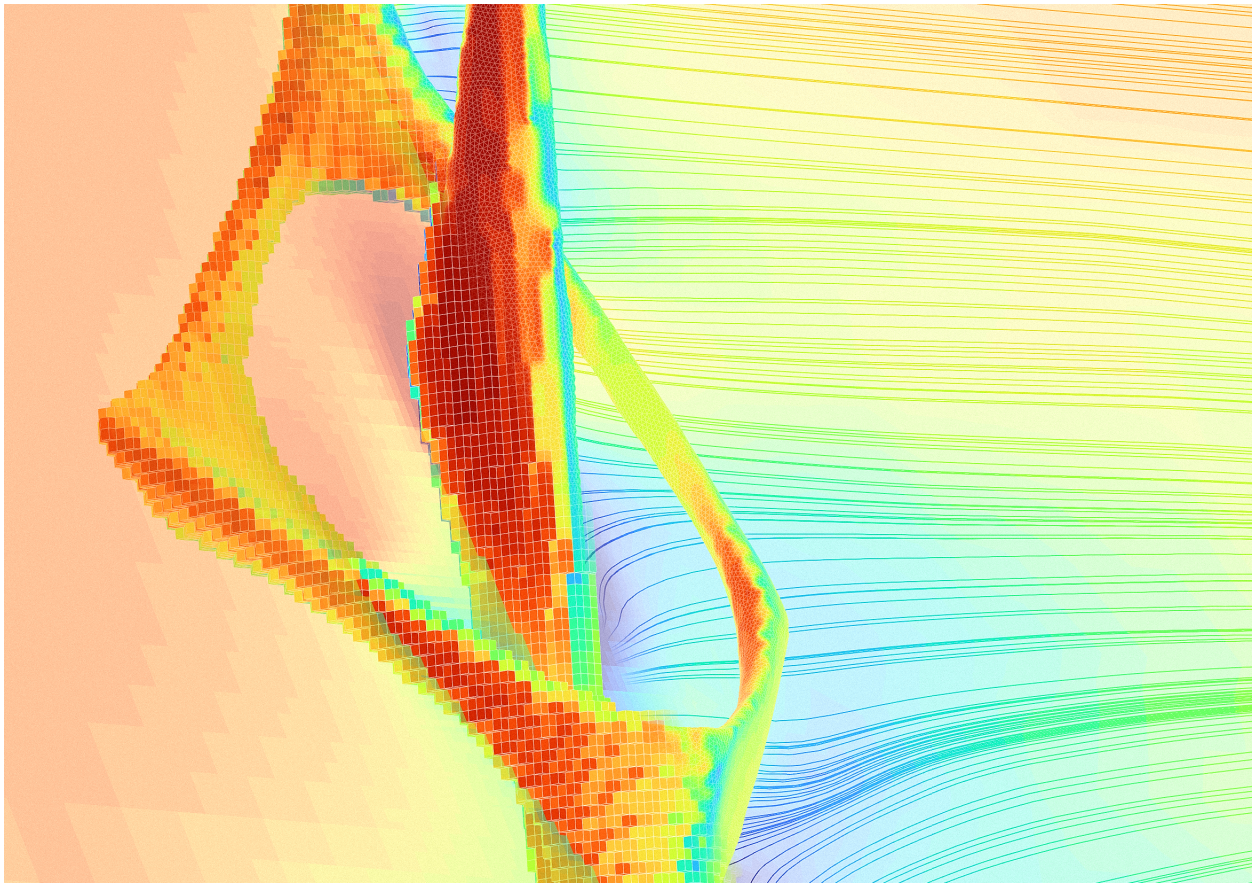

Early phase evaluation of building wind interaction for structural design

Validation and integration of IBOFlow:
An Immersed Boundary flow solver, in a structural design context

Master's thesis in Structural Engineering and Building Technology

AXEL GRAMPP

DEPARTMENT OF ARCHITECTURE AND CIVIL ENGINEERING
DEPARTMENT OF MECHANICS AND MARITIME SCIENCES
CHALMERS UNIVERSITY OF TECHNOLOGY
Gothenburg, Sweden 2025
www.chalmers.se

Master's thesis 2025

Early phase evaluation of building wind interaction for structural design

Validation and integration of IBOFlow:
An Immersed Boundary flow solver, in a structural design context

AXEL GRAMPP

CHALMERS
UNIVERSITY OF TECHNOLOGY

Department of Architecture and Civil Engineering
Department of Mechanics and Maritime Sciences
Chalmers University of Technology
Gothenburg, Sweden 2025

Early phase evaluation of building wind interaction for structural design
Validation and integration of IBOFlow:
An Immersed Boundary flow solver, in a structural design context

AXEL GRAMPP

Supervisor: Martin Fröderberg, Tyréns Sverige AB
Supervisor: Gaetano Sardina, Department of Mechanics and Maritime Sciences
Examiner: Mats Ander, Department of Architecture and Civil Engineering

Master's Thesis 2025
Department of Architecture and Civil Engineering
Department of Mechanics and Maritime Sciences
Chalmers University of Technology
SE-412 96 Gothenburg
Telephone +46 31 772 1000

Cover: Surface pressure visualization made in Paraview showing the transition between a discretized Immersed Boundary shape and the base surface.

Typeset in LaTeX
Printed by Chalmers Reproservice
Gothenburg, Sweden 2025

Early phase evaluation of building wind interaction for structural design
Validation and integration of an Immersed-Boundary flow solver in a structural design context

AXEL GRAMPP
Department of Architecture and Civil Engineering
Chalmers University of Technology

Abstract

Wind is a major horizontal force on structures. Due to its complex and highly variable behaviour, reliance on design codes such as Eurocode 1991-1-4 is necessary for predicting wind effects. However, such codes cannot fully account for all, infinitely variable types of structures and their resulting aerodynamic responses. The dominant alternative, wind-tunnel testing, provides detailed results but remains costly and time-consuming. In parallel, Computational Fluid Dynamics (CFD) has gained increasing credibility as a complementary approach for wind analysis.

This thesis explores the application of IBOFlow, an in-house CFD flow-solver developed by Fraunhofer-Chalmers Centre, in an structural design context. Through a validation study, IBOFlow was shown to achieve favorable prediction performance and overall agreement with benchmark wind-tunnel data. Subsequently, a series of Case Studies further explored its integration into early-stage design workflows, illustrating its ability to complement code-based approaches and support early-stage design exploration.

The results indicate that the integrated IBOFlow method can provide valuable predictions, while reducing the time needed for setup and calculation. The study concludes that an immersed-boundary CFD approach, when validated and integrated with design tools, can potentially offer a practical and accessible means to enhance early-phase wind assessment of complex structures for structural engineers.

Keywords: Eurocode 1991-1-4, Wind effects, Structural Design, Optimization, Early Stage, CFD, Complex geometry

Early phase evaluation of building wind interaction for structural design
Validation and integration of an Immersed-Boundary flow solver in a structural design context

AXEL GRAMPP
Department of Architecture and Civil Engineering
Chalmers University of Technology

Sammanfattning

Vind utgör en av de främsta horisontella lasterna på byggnader och konstruktioner. På grund av dess komplexa och varierande beteende är det nödvändigt att tillämpa standarder, såsom Eurokod 1991-1-4, för att uppskatta vindlaster. Dessa standarder har dock begränsningar och kan inte fullt ut täcka alla tänkbara byggnadsformer och deras aerodynamiska respons. Det främsta alternativet, vindtunneltester, kan ge detaljerade resultat men är både kostsamt och tidskrävande. Samtidigt har metoder baserade på Computational Fluid Dynamics (CFD) fått ökad trovärdighet som ett kompletterande verktyg för vindanalys.

Detta examensarbete undersöker användningen av IBOFlow, en CFD-metod utvecklad av Fraunhofer-Chalmers Centre, i ett *Structural Design*-sammanhang. Genom en valideringsstudie visades att IBOFlow har god förmåga att uppskatta tryckkoefficienter, och överensstämmer överlag med referensdata från vindtunneltester. Därefter utforskades integration av metoden i tidiga designskeden genom en serie *Case Studies*, som illustrerade hur metoden kan komplettera Eurocode-baserade metoder och ge vägledning i en tidig designprocess.

Resultaten visar att den integrerade IBOFlow-metoden kan ge värdefulla resultat, samtidigt som den begränsar tidsåtgången för *Setup* och beräkning. Studien drar slutsatsen att en *Immersed Boundary*-baserad CFD-metod, när den är validerad och integrerad i designverktyg, kan utgöra ett praktiskt och tillgängligt stöd för konstruktörer vid tidig vindanalys av komplexa strukturer.

Keywords: Eurocode 1991-1-4, Wind effects, Structural Design, Optimization, Early Stage, CFD, Complex geometry

Acknowledgements

Firstly, I want to express my gratitude to my supervisors Martin Fröderberg at Tyréns and Dr. Gaetano Sardina at the division of fluid mechanics, as well as my examiner Senior Lecturer Mats Ander. I also want to sincerely thank Dr. Andreas Mark at FCC, your support and introduction to the software was indispensable for this thesis.
Thank you to all my colleagues at Tyréns, for the feedback and nice discussions during lunchtimes at the office.
Lastly, I want to thank my girlfriend for all of the continuous encouragement and support, I simply could not have done it without you.

Axel Grampp, Gothenburg, June 2025

Contents

List of Figures

List of Tables

Nomenclature

Below is the nomenclature of parameters, constants, non-dimensional numbers and variables that have been used throughout this thesis, in order of appearance.

F	Force [N]
m	Mass [kg]
a	Acceleration [m/s^2]
V	Volume [m^3]
A	Area [m^2]
ρ	Density [kg/m^3]
$\vec{u}$	Directional velocity [m/s]
u	Fluid velocity [m/s]
t	Time [s]
q_{heat}	Heat flux [W/m^2]
k	Thermal Conductivity [W/(m·K)]
T_k	Temperature [K]
b	Body force [N/m^3]
f	External forces [N/m^3]
σ	Stress tensor [N/m^2]
p	Pressure forces [N/m^2]
T	Stress deviator tensor [N/m^2]
p_0	Integration constant [N/m^2]
c_p	Pressure coefficient [-]
$\bar{u}$	Sum of fluid velocity [m/s]
U	Averaged mean fluid velocity [m/s]
$\bar{p}$	Sum of fluid pressure [N/m^2]
P	Averaged mean fluid pressure [N/m^2]
$\bar{T}$	Sum of fluid stresses [N/m^2]
T	Averaged mean fluid stresses [N/m^2]
τ	Fluid stresses [N/m^2]
Re	Reynolds number [-]
L	Characteristic length scale [m]
u^*	Friction velocity [m/s]
z	Height [m]

z_0	Surface roughness [m]
u_{ref}	Reference wind velocity [m/s]
κ	von Karman constant [-]
v_m	Mean wind velocity [m/s]
v_b	Characteristic wind velocity [m/s]
c_r	Roughness factor [-]
c_o	Orography factor [-]
k_r	Terrain factor [-]
$z_{0,II}$	Surface roughness of terrain category II [m]
z_{ref}	Reference height [m]
α	Roughness coefficient [-]
σ_v	Standard deviation of wind speeds [m/s]
I_v	Turbulence intensity [-]
I	Turbulence intensity [-]
k_I	Turbulence factor [-]
$\hat{U}$	Peak gust wind speed [m/s]
g	Peak factor [-]
G	Gust factor [-]
k_p	Peak factor [-]
q	Surface pressures [N/m^2]
$c_{p,10}$	Pressure coefficient [-]
$c_{p,1}$	Pressure coefficient [-]
C_μ	Coefficient for ABL model [-]
C_1	Calibration coefficient [-]
C_2	Calibration coefficient [-]
q_b	Basic velocity pressure [N/m^2]
q_p	Peak velocity pressure [N/m^2]
h_{ave}	Surrounding average building height [m]
h_{dis}	Displacement height [m]
q_{sim}	Surface pressures from IBOFlow simulation [N/m^2]
q_{diff}	Difference in surface pressure between code calculation and simulation [N/m^2]
c_{diff}	Factor between q_{sim} and q_{diff} [-]
M	Moment [N·m]
r	Moment arm [m]
B	Building base width [m]
H	Building height [m]
C_M	Overturning moment coefficient [-]
q_h	Velocity pressure [N/m^2]
$C_{M,Rel}$	Normalized C_M against baseline structure [-]

1
Introduction

Wind generally represents one of the main horizontal loads affecting a building, which in particular holds true for slender structures such as high-rises or bridges. Well known for its complex behavior, wind and fluid dynamics is a full discipline and field of research of its own. Yet, it is expected of the structural engineer to grasp it's behavior enough to apply design codes and standards, such as Eurocode. Building design codes consist of years and years of aggregated empirical data, knowledge, experience, and tests performed by experts, made accessible for engineers by condensing the knowledge into suitably rigid procedures.

Between wind and other environmental or physical loads, aesthetics, economic constraints, sustainability and proper material usage, structural engineers operate within the balance of a considerable amount of factors while yet making designs that fulfill both structural integrity and serviceability demands of the completed structure. Reliance on code is necessary in order to facilitate design procedures that does not go beyond human comprehension in sheer volume of factors to consider, and yet maintains attention to key aspects and importantly – safety.

However, codes and simplifications inherently cannot account for all, infinitely variable and specific types of structures. In cases where a building for any reasons is deemed to lie outside established design code classification, wind tunnel studies can be performed (Boverket, 1997) to help determine the wind load effects.

Although substantially less widely accepted than wind tunnel studies, numerical CFD (Computational Fluid Dynamics) simulations have helped establish the field of Computational Wind Engineering (CWE), and is still gaining credibility as well as accessibility and usabilty in parallel with modern computer hardware development (Simiu et al., 2019). In contrast to wind tunnel studies, numerical simulations can be significantly cheaper and faster, enabling more iterations and optimization. However, the technical complexity of setting up reliable simulations remain barriers for structural engineers outside the CFD domain.

Nevertheless, the demand and potential of applying numerical simulations to structural design in exceptional and complex cases – whether to directly inform design, iterate and optimize or to guide code usage – remains (Simiu et al., 2019). If the barriers of complexity within setup and configuration can be reduced, numerical simulation could become a more integrated tool informing early-stage architectural and structural decisions.

1.1 Background

The fundamentals of science-based wind design for structures, and the core of the resulting building codes, was largely established in the late 19th to mid 20th century (Solari, 2019). A significant boost in the interest of understanding wind effects were initially driven by the development of increasingly longer and slender bridges, as well as taller and less heavy buildings, both of which were built on the advent of structural iron and steel. The abundantly famous Tacoma Narrows suspension bridge collapse of 1940 clearly illustrated the gaps in knowledge about wind effects. Often to this day attributed to a plain oversight in natural mechanical resonance of the bridge geometry, the actual cause of the collapse was due to an at the time unknown effect; flutter, specifically in torsion (Bilah et al., 1990). The overall aerodynamic properties of the bridge deck provided a basis for unfavorable positive feedback between deflection and aerodynamic forces.

Key development during the middle 20th centaury can be attributed to wind engineer Professor Alan Garnett Davenport, one of the most well known names in wind engineering and whose research has vast relevance to this day (Solari, 2019).
His work was fundamental in two main categories. Firstly; defining the concept of statistical probability of maximum and mean wind speeds depending on location, surrounding context, and terrain roughness in conjunction with real atmospheric measurements. Secondly; determining wind-induced dynamic response of buildings and it's relation to turbulence, drag forces as well as gust effects. The link of associated effects between site and climate, wind speed, gusts and the resulting aerodynamic and dynamic forces, is referred to as a Davenport chain.

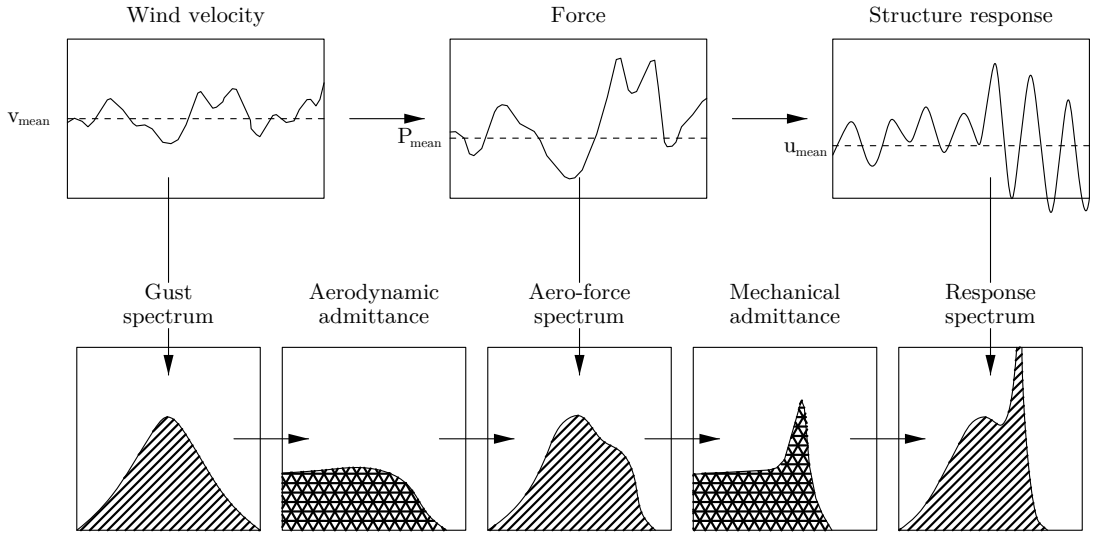

Figure 1.1: Davenport chain of wind speed, probability and response.

His expansion of knowledge led to key involvement in determining wind response of unprecedented tall and light in New York and Chicago during the 1960's and 70's. In addition, during his research, he aptly and fittingly pointed out the need for wind tunnel testing in cases of structures that – due to context or geometry – lacked sufficient empirical precedent.

1.1.1 Design standards and Eurocode

The European building standard, collectively called Eurocode, is a large compendium of design standards to estimate key effects on structures and their response. Its conception has it's origin in the demand for harmonizing different structural design guidelines across Europe. Davenport is just one of many researches whose work made its way into different national standards, eventually harmonized into Eurocode, with remaining continuity directly from his research.

Eurocode 1: Actions on structures – Part 1–4: General actions – Wind actions, or Eurocode 1991-1-4 (EN-1991-1-4, 2005), covers how to estimate wind effects of common built structures. The general procedure is to first establish the mean (statistical) wind velocity based on location and context, and then the *velocity pressure* (in a fluid mechanics context called dynamic pressure). Finally, the peak surface pressure and design wind loads can be determined in order to design the lateral bracing and the external cladding.

Eurocode still to an extent provides procedures for designing less typical buildings and slender structures subject to a wider range of dynamic effects, but generally increases the level of abstraction and uncertainties. The inherent limitation of codes needing to balance usability and simplicity, and narrowing down the amount of treated structures leads to the inevitable cases where wind tunnel testing becomes necessary. Current Eurocode itself states that for certain structures, such as buildings above 200 meters tall, situated in complex environments or subject to torsional vibration, wind tunnel testing is recommended.

1.1.2 Wind Tunnel Test and Computational Wind Engineering

A properly calibrated wind tunnel test is the dominant benchmark alternative when codes is deemed unable to accurately represent the studied structure. (Simiu et al., 2019) The drawbacks are time, cost and requirement of specific expertise and equipment, which presents an substantial obstacle in accessibility.

At the end of the 1960s, using numerical methods and early computers to calculate three-dimensional fluid flows was shown possible, which in time led to the advent of CFD (Simiu et al., 2019). These numerical methods can collectively and briefly be described as ways to approximate solutions to the *Navier-Stokes* equations; in essence fundamental partial differential equations that describe the motions of fluids.

Solving the numerical methods can be highly computationally intensive, and are often performed in High-Performance-Computing (HPC) Clusters (Elmisaoui et al., 2024). Another fundamental drawback is that the simulation results depends on which calculation approach or model is selected. Inlet conditions, 3D model, details and mesh, and other *chosen* parameters can all have consequential effects on the results (Simiu et al., 2019). Useful results therefore depends on a correct and precise setup performed by a knowledgeable expert, which limits the general accessibility of CFD simulations. One advantage compared to wind tunnels is the overall time needed for setup. However, due to results being contingent on chosen parameters, CFD is generally and advisably only used for informing design at earlier stages.

1.1.3 Context

Vertikal Komposition (English: *Vertical Composition*) is a public artwork sculpture designed by Swedish artist Arne Jones (1914 – 1977), with an original version in copper built 1952 in Lund (Statens Konstråd, 2023). From its completion, *Vertikal Komposition* lived a tough life, enduring harsh weather, attempts to steal it, a truck collision, and ultimately succumbing to a storm that toppled it in 2011.

Figure 1.2: Original *Vertikal Komposition* sculpture

In 2023, a 7.5 meter tall replica was constructed close to the original site, and the original artwork's "*confidence and an unbridled sense of freedom*" (Statens Konstråd, 2023) once again grace the public place in which it is situated.

The complex geometric shape and relative slenderness brought a noteworthy challenge during design and dimensioning of the sculpture's load bearing structure. It was deemed likely to generate a range of different aerodynamic effects with potential interaction with the slender structure's natural resonance frequency. The closest equivalent in building code with similarities in slenderness, was to follow a design procedure normally used when designing industrial chimney stacks. Additionally, the predominantly triangular cross-section of the sculpture lacks direct support in code.

To better understand the structure's behavior in wind, a wind tunnel or CFD simulation could have been performed. However, with an estimated cost between 250.000 and 400.000 SEK for a certified and reliable result, this was deemed too expensive for the project's budget.

The final design is based on qualified and careful assumptions, together with leading edge empirical studies of wind effects on geometry not yet covered by Eurocode. With safety factors included, it is unlikely the final design is inadequate. Yet, the uncertainties in the approach together with the low accessibility of numerical simulations illustrates the limits and challenges of relying on code and empirical data for complex structural design cases, which inspired this thesis.

1.2 Aim

Given the increasing accessibility of computational power (modern consumer hardware) as well as current trends of emphasis on optimized structures and important early-stage design decisions, the potential of CWE and CFD motivates further exploration. This thesis aims to develop and validate an integrated, accessible CFD method for structural design that complements empirical codes such as Eurocode in early-phase analysis of complex geometry. It attempts to address the gap between design codes, wind tunnel studies and existing CFD alternatives by developing a method that balances accessibility, accuracy, and computational efficiency.
Specifically, the goal is to evaluate complete software libraries of CFD-based simulation methods independently, as well as integrated into hypothetical design scenarios in a series of Case Studies. The integrated approach relies on developing an interface between design softwares commonly used by engineers and the CFD libraries. The interface and integrated method as well as the results should be evaluated on accuracy, user friendliness and accessibility and the ability to assist design choices, compared to empirical code usage. Finally, the aim is to conclude whether the explored integrated method offer potential improvements over current approaches.

Research questions:

- Provide an overview of fundamental fluid mechanics, and its relation to empirical design codes, particularly Eurocode.
- Outline the current challenges going from empirical data to numerical methods.
- Test and validate simulation methods in a structural design context.
- Implement, and test new CFD methods and evaluate the potential as well as relevance.

1.3 Methodology

The methodology revolves around applying IBOFlow, a flow solver developed at FCC (Fraunhofer-Chalmers Center). The inherent benefits of IBOFlow and its Immersed Boundary basis has driven its recent application in research aimed primarily at increasing accessibility of numerical methods in urban wind flow simulations, although for architects and planners rather than structural engineering applications (Vanky et al., 2024).

The thesis also establishes the interdisciplinary link between structural engineering, wind engineering, and CFD through describing fluid mechanics fundamentals. Current code-based design procedures are also examined, highlighting their inherent challenges and limitations.

IBOFlow is then validated for structural engineering purposes; in practical simulating a structure (building) and comparing the results with wind tunnel data in order to give the

simulated method credibility which is important in order to prove the overall usability of the method. The setup of IBOFlow for all simulations is largely done through Python scripts, written in VSCode and Python Version 3.10. Finally, Case Studies demonstrate how the IBOFlow based method and simulated results can inform code usage and early-phase design.

1.4 Limitations

CFD methods have the ability to consider explicitly modeled and highly complex environments; this study will focus on either simulating singular structures *or* the surrounding environment.

For the structure itself, the main results of the simulation will concern surface pressures and their subsequent statical loads, as well as their relation to Eurocode 1991-1-4. Due to some on the inherent properties of the simulation, the primary focus will be on static forces rather than dynamic effects. Beyond numerical results, the simulation will be qualitatively evaluated on credibility, as well as accessibility and usefulness.

FSI (Fluid Structure Interaction) and other highly detailed simulation results is beyond scope for this study, as well as direct integration with FEM software, but remains as a natural extension of the thesis theme.

2

Fluid mechanics fundamentals

While a thesis written solely within the field of fluid mechanics might simply state the Navier-Stokes equations directly (See Section 2.1.3), this chapter's purpose is to frame fluid mechanics specifically for structural engineers. As will be made more evident, several fluid mechanic principles are present in design codes (e.g., Eurocode), though this is not always apparent. Importantly, fluid mechanics forms the fundamental basis for both codes based approaches and numerical simulations, therefore also also serving as the common link between the two.

2.1 Navier-Stokes Equation

Navier-Stokes equation describes the motion of a fluid continuum as an extension of Newtons second law of motion (Equation 2.1); the relation between force, mass and acceleration:

$$\vec{F} = m\vec{a} \tag{2.1}$$

2.1.1 Conservation of mass

Consider an arbitrary enclosed and constant control volume V as a subsection of an fluid continuum, used as a reference point. The surface of the control volume, A, is permeable, allowing fluid to flow in and out. The rate of change (Mass flux) leaving the control volume across the surface A, measured in mass M is:

$$\frac{d}{dt}M = -\int_A \rho\ \vec{u}\ \cdot \hat{n}\ dA \tag{2.2}$$

where $\vec{u}$ is the fluid velocity and $\hat{n} = (\hat{n_1}, \hat{n_2}, \hat{n_3})$ is the unit normal vector of the surface.
Expression 2.2 can be further developed with M expressed as the integral of density over the volume V:

$$\frac{d}{dt}\int_V \rho\ dV = -\int_A \rho\ \vec{u}\ \cdot \hat{n}\ dA \tag{2.3}$$

By incorporating the derivative over time into the integral, and applying the Divergence Theorem to the Mass flux (right hand side), equation 2.3 can be rewritten from a surface integral to a volume integral as Equation 2.4:

$$\begin{aligned} \int_V \frac{d\rho}{dt}\ dV &= -\int_A \rho\ \vec{u}\ \cdot \hat{n}\ dA \\ \int_V \frac{d\rho}{dt}\ dV &= -\int_V \nabla \cdot \rho\ \vec{u}\ dV \\ \int_V \left(\frac{d\rho}{dt} + \nabla \cdot \rho\ \vec{u}\right)\ dV &= 0 \end{aligned} \tag{2.4}$$

Since the original control volume V was chosen arbitrarily as a subsection of the fluid continuum, it could also be any other volume within the fluid. As to not violate mass-conservation, the integrand must vanish ($= 0$), which can be summarized by what is usually called the continuity equation, written without the integrand:

$$\frac{\delta \rho}{\delta t} + \nabla \cdot \rho \ \vec{u} = 0 \tag{2.5}$$

Often, it's useful to simplify this statement further depending on the context. At typical air speeds encountered by buildings, air can be considered as *incompressible*, meaning that the density ρ is considered constant. This is in contrast to higher air velocities reaching 100 m/s and above (Simscale, 2024), where compressibility becomes crucial, particularly in design of jet planes approaching Mach 1 (331 m/s).

With a constant but non-zero density ρ, the simplest expression of conservation of mass is obtained:

$$\nabla \cdot \vec{u} = 0 \tag{2.6}$$

Solely for the sake of familiarity to building engineers, this could be related to Fouriers law, Equation 2.7:

$$q_{heat} = -k \nabla T_k \tag{2.7}$$

However, where $\nabla \cdot q > 0$ indicates a heat source, and conversely $\nabla \cdot q < 0$ indicate a heat sink (Fagerström, 2019), the equivalent situation in the mass conservation equation for incompressible fluids (Equation 2.6) would imply a "mass source" or "mass sink" which for all practical purposes is nonsensical.

2.1.2 Conservation of momentum

A body force is a force that acts throughout the volume of a body, defined as:

$$b = \int_V f \ dV \tag{2.8}$$

Newton's second law defined for a small volume element ($V \to 0$) with a body force (Barber, 2010) is defined as:

$$b = \rho \ \frac{du}{dt} \tag{2.9}$$

Here acceleration a is represented by (du/dt), where $u = u(x, y, z, t)$. Expanding the derivatives of (du/dt) in Equation 2.9 using the chain rule, Equation 2.9 can be written as:

$$\begin{aligned} b &= \rho \ \left(\frac{\delta \vec{u}}{\delta t} + \frac{\delta \vec{u}}{\delta x}\frac{\delta x}{\delta t} + \frac{\delta \vec{u}}{\delta y}\frac{\delta y}{\delta t} + \frac{\delta \vec{u}}{\delta z}\frac{\delta z}{\delta t} \right) \\ &= \rho \ \left(\frac{\delta \vec{u}}{\delta t} + \vec{u} \cdot \nabla \vec{u} \right) \end{aligned} \tag{2.10}$$

The body forces for a fluid consists of two components: fluid stresses and external forces which can be written as:

$$b = \nabla \cdot \sigma + \vec{f} \tag{2.11}$$

The fluid stresses are written as the divergence of the stress tensor $\nabla \cdot \sigma$. Equation 2.7 and the following expansion can be useful to intuitively grasp how $\nabla \cdot \sigma$ represents *to which extent the stress tensor behaves like a sink or a source*, which results in a sink or a *source of momentum*, or otherwise known as: a force.

The stress tensor is a *third order symmetric tensor*, expanded in Equation 2.12 to show stresses and shear in all principal directions, and separated into two tensors, the *hydrostatic stress tensor* and the *stress deviator tensor*:

$$\begin{aligned} \sigma &= \begin{pmatrix} \sigma_{xx} & \tau_{xy} & \tau_{xz} \\ \tau_{yx} & \sigma_{yy} & \tau_{yz} \\ \tau_{zx} & \tau_{zy} & \sigma_{zz} \end{pmatrix} \\ &= \begin{pmatrix} -p & 0 & 0 \\ 0 & -p & 0 \\ 0 & 0 & -p \end{pmatrix} + \begin{pmatrix} \sigma_{xx}+p & \tau_{xy} & \tau_{xz} \\ \tau_{yx} & \sigma_{yy}+p & \tau_{yz} \\ \tau_{zx} & \tau_{zy} & \sigma_{zz}+p \end{pmatrix} \end{aligned} \tag{2.12}$$

The volumetric stress tensor represents the forces that determine the body volume – these are the pressure forces p. The stress deviator tensor represent the forces which determine the body deformation and movement. We can summarize this separation by:

$$\sigma = -pI + T \tag{2.13}$$

where T represents the stress deviator tensor. Finally, in Equation 2.11 we can substitute b with Equation 2.10 and σ with Equation 2.13 which results in:

$$\begin{aligned} b &= \nabla\sigma + \vec{f} \\ \rho\left(\frac{\partial \vec{u}}{\partial t} + \vec{u}\cdot\nabla\vec{u}\right) &= \nabla(-pI+T) + \vec{f} \\ \rho\left(\frac{\partial \vec{u}}{\partial t} + \vec{u}\cdot\nabla\vec{u}\right) &= -\nabla p + \nabla\cdot T + \vec{f} \end{aligned} \tag{2.14}$$

2.1.3 Final Navier-Stokes equation

To obtain the common form of the Navier-Stokes equations from Equation 2.14, a key assumption is introduced. Firstly, air and water are *Newtonian* fluids, meaning that change in velocity (velocity gradient) is linearly proportional to the shear stress (Gibiansky, 2011). This proportionality constant is known as the dynamic viscosity μ, which for *incompressible*, *Newtonian* fluids allows the divergence of stress $\nabla \cdot T$ to be expanded and rewritten as:

$$\nabla \cdot T = \mu\nabla^2 u \tag{2.15}$$

The detailed derivation of Equation 2.15 lies beyond this chapter's (and thesis') scope, but can be found in the references Gibiansky (2011) and Waterman (2024), upon which the other parts of this chapter are based on. With Equation 2.15, the common form of the Navier-Stokes equation for incompressible Newtonian fluids can be written as Equation 2.16:

$$\begin{aligned} \text{Mass conservation:} \quad & \nabla\cdot\vec{u} = 0 \\ \text{Momentum conservation:} \quad & \rho\left(\frac{\partial \vec{u}}{\partial t} + \vec{u}\cdot\nabla\vec{u}\right) = -\nabla p + \mu\nabla^2\vec{u} + \vec{f} \end{aligned} \tag{2.16}$$

Equation 2.16 consist of two parts; the first part of Equation 2.16 is a statement of the conservation of mass, which describes the fluid kinematic behavior. The second part of Equation 2.16 represents the expanded form of Newton's second law for a fluid, detailing the relationship between mass, acceleration and the forces (pressure, viscous, external forces) acting upon the fluid continuum.

$$\overbrace{\underbrace{\rho}_{\text{Fluid density}}}^{\text{Mass}} \cdot \overbrace{\underbrace{\left(\frac{\partial \vec{u}}{\partial t}\right)}_{\substack{\text{Change in velocity} \\ \text{(Unsteady acceleration)}}} + \underbrace{(\vec{u} \cdot \nabla)\vec{u}}_{\substack{\text{Fluid speed and direction} \\ \text{(Convective acceleration)}}}}^{\text{Acceleration}} = \overbrace{\underbrace{-\nabla p}_{\text{Pressure gradient}} + \underbrace{\mu \nabla^2 \vec{u}}_{\text{Viscous forces}} + \underbrace{\vec{f}}_{\text{External forces}}}^{\text{Force}}$$

It is worth emphasizing that the Navier-Stokes equations are highly complex; they constitute a set of highly non-linear, partial differential equations, primarily due to the convective acceleration term and the viscous forces which involve second-order derivatives. Indeed, one of the famously unsolved problems in mathematics is the Navier-Stokes existence and smoothness problem in three dimensions. (Clay, 2025)

2.2 Bernoulli's Equation

While the Navier-Stokes equations provide a fundamental description of fluid motion, the Navier-Stokes equations in isolation are not very practical, especially not for structural engineers trying to quickly estimate wind loads on a building. However, for many common fluid flow scenarios, significant and justifiable simplification can be made, in order to yield a more practical mathematical expression for fluid mechanics, namely the Bernoulli's equations.

The difference in viscosity between water and air is intuitively recognized; dragging your hand through water creates a noticeable resistance from the neighboring fluid due to viscosity. (Gibiansky, 2011) Building on this intuition, the Navier-Stokes equations can be simplified under specific conditions. For a vanishingly small "parcel" of incompressible fluid (like air at typical air speeds) flowing in *one dimension* along a *streamline*, see Figure 2.1, we can assume the viscous effect to be zero (inviscid). Furthermore, it is assumed that the flow is steady, and that the unsteady acceleration term vanishes.

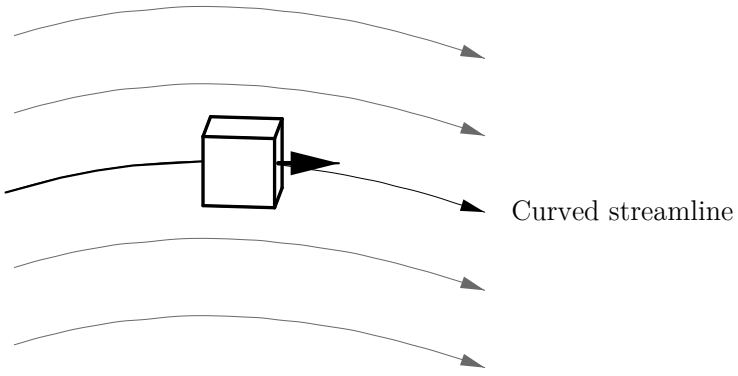

Figure 2.1: Parcel of air (cube) flowing along 1D streamline

With these assumptions, the Navier-Stokes equations in one dimension (derivative instead of gradient) can be written as:

$$\underbrace{\rho}_{\text{Fluid density}} \cdot \underbrace{\vec{u}\,\frac{d\vec{u}}{dx}}_{\text{Fluid speed and direction}} = \underbrace{-\frac{dp}{dx}}_{\text{Change in pressure}} \tag{2.17}$$

Rearranging and integrating this simplified equation yields:

$$\begin{aligned} &\rho\vec{u}\frac{d\vec{u}}{dx} + \frac{dp}{dx} = 0 \\ &\text{Integrate:} \\ &\frac{1}{2}\rho\vec{u}^2 + p = p_0 \end{aligned} \tag{2.18}$$

Bernoulli's equation written out in detail is:

$$\underbrace{\frac{1}{2}\rho\vec{u}^2}_{\substack{\text{Dynamic pressure} \\ \text{(Velocity pressure)}}} + \underbrace{p}_{\text{Static pressure}} = \underbrace{p_0}_{\text{Integration constant}} \tag{2.19}$$

This equation implies that under the stated assumptions, the sum of dynamic pressure and static pressure is constant along a streamline. Consequently, if a "parcel" of air experiences an increase in velocity, its dynamic pressure increases, leading to a proportional decrease in static pressure. Conversely when the "parcel" slows down, the dynamic pressure decreases leading to a increase in static pressure.

While actual wind flow around a building is not entirely in-viscid (though viscosity is small) and certainly not one-dimensional (it is highly three dimensional), the overall implications of Bernoulli's equation remains relevant. In fact, wind loads calculated in Eurocode have a direct connection to the static pressure forces in Bernoulli's equation, making it fundamental to the wind load calculations (EN-1991-1-4, 2005).

It is also common to relate pressures on a building surface to the dynamic pressure of the free-stream wind velocity, where the free-stream wind refers to the undisturbed wind upstream of the building (Simiu, 2019). The relationship between the pressure at any location of the building surface and the free-stream dynamic pressure is described by the non-dimensional pressure coefficient c_p, defined as:

$$c_p = \frac{p - p_0}{\frac{1}{2}\rho\ \vec{u}^2} \tag{2.20}$$

2.3 Boundary layers

Air viscosity is as previously stated small; nevertheless, it still has an important role in the formation of boundary layers (Simiu, 2019). A boundary layer is a layer of fluid in the vicinity of a surface (such as a building facade or terrain), where the motion is affected by the friction between the fluid and the surface, making its characteristics distinctly different from the free-stream air.

As air flows over a surface, the velocity in the direct vicinity of the surface is zero, known as a "no-slip" condition; the air effectively "sticks" to the surface (Simiu, 2019). Due to the small but nonetheless influential viscosity of air, internal friction forces slow adjacent fluid layers down causing the velocity to gradually increase from zero to the velocity of the free-stream air.

The boundary layer can also detach from the surface, known as flow separation. When the air slows down (due to surface and viscous friction), the pressure increases. At the point when the kinetic energy of the air is insufficient to overcome the increased pressure, the flow slows further and eventually reverses, leading to the detachment of the boundary layer (Simiu, 2019), as illustrated by Figure 2.2:

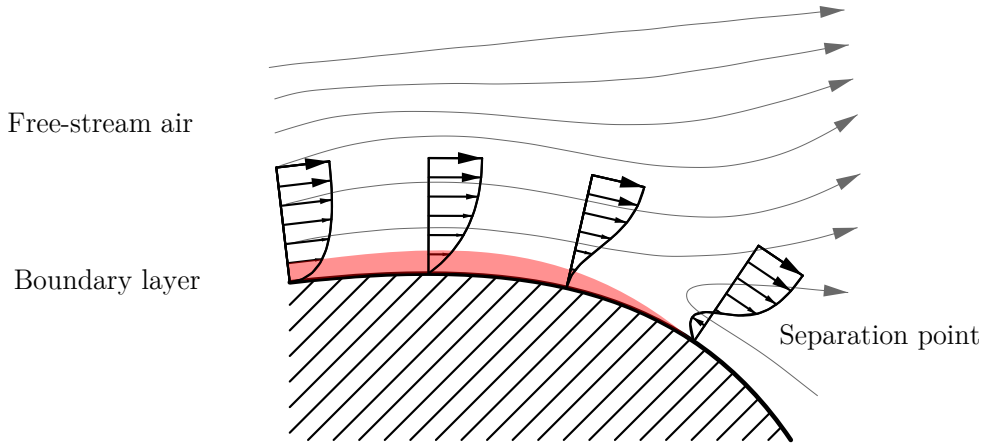

Figure 2.2: Formation of flow separation

Downstream of a separated boundary, especially behind bluff bodes (bluff: in a aerodynamic sense "blunt") such as buildings, a *wake* is formed, characterized by swirling motions and vortices generated from the shear between air layers with opposing (reversed) velocities. Its influence gradually dissipates as the flow mixes with the free-stream air.

2.4 Turbulence

The previous Section 2.3 hints at *turbulence*, describing the wake behind a building as "characterized by swirling motions and vortices". Collectively, these can be referred to as "turbulent" structures and in fact, in terms of defining turbulence this is essentially as close as it gets. Indeed, an universally accepted, exact (mathematical) definition of turbulence does not exist. (George, 2013). Rather, it is mainly defined by its characteristics, which are the irregular and unstable flow patterns, swirling vortices and *eddies*, superimposed at many different temporal and physical scales (Andersson, 2024).

Turbulence is also dissipative, an essential feature indicating that if no energy is added, it will eventually decay. The kinetic energy from the largest swirling structures is transferred to successively smaller and smaller swirls until it is small enough to dissipate into the fluid internal energy through viscosity, which is referred to as the *energy cascade*, see Figure 2.3

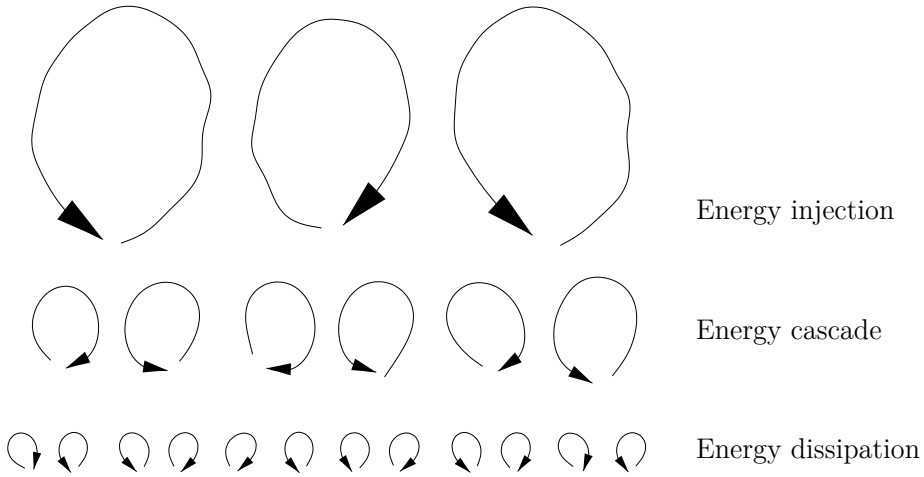

Figure 2.3: Energy cascade

Due to the chaotic nature of turbulence, it can be practical to consider the flow as consisting of two part: a mean (average) component and the fluctuating (turbulent) component. (Davidson, 2024), illustrated as:

$$\begin{aligned} \bar{u} &= U + u \\ \bar{p} &= P + p \\ \bar{T} &= T + \tau \end{aligned} \tag{2.21}$$

This *Reynolds decomposition* expresses any instantaneous motion as a sum of its time-averaged mean components (U, P and T) and its fluctuating components (u, p and τ). Lastly, on the topic of turbulence is it worth stating that any wind affecting a building *will* be turbulent (Simiu, 2019), and that the turbulence can have an immense impact (for example Figure 2.4 and the preceding explanation).

2.4.1 Reynolds number

The *Reynolds number* (Re) is an important non-dimensional parameter in fluid mechanics, representing the ratio between inertial and viscous forces (Simiu, 2019). While the Navier-Stokes equations describes this relationship as well, the Reynolds number Re, (derivation shown in Simiu, 2019), can be used to more concisely categorize and predict fluid flow phenomena:

$$Re = \frac{\rho U^2 L^2}{\mu U L} = \frac{\rho U L}{\mu} \tag{2.22}$$

Here, ρ is the fluid density, U is the characteristic flow velocity, L is a characteristic length scale (e.g. the width of a building), and μ is the dynamic viscosity of the fluid.
At lower Re, viscous effects dominate and the flow tends to be *laminar* (smooth). Conversely, at higher Re, inertial effects dominate and the flow tends to be turbulent (Simiu, 2019).

The transition between smooth, laminar and undisturbed flow to turbulent flow was studied by Osborne Reynold (1842 - 1912), hence the naming of the Reynolds number (Simscale, 2024). At low velocities (and lower Re numbers), the fluid viscosity dampen small disturbances that may arise. However, at higher velocities (and higher Re numbers), the increased

inertial forces overcome this viscous damping, feeding turbulent energy into the formation of turbulent structures. In the context of wind affecting buildings, it is relevant for two reasons (Simiu, 2019):

Firstly, laminar and turbulent air have different properties and movement patterns, which can affect local pressures and wind loads on building surfaces.

Secondly, at intermediate Reynold numbers, the formation of turbulent structures can be periodic, illustrated by Figure 2.4. Periodic *vortex shedding* can cause unsteady and periodic forces loads on a building.

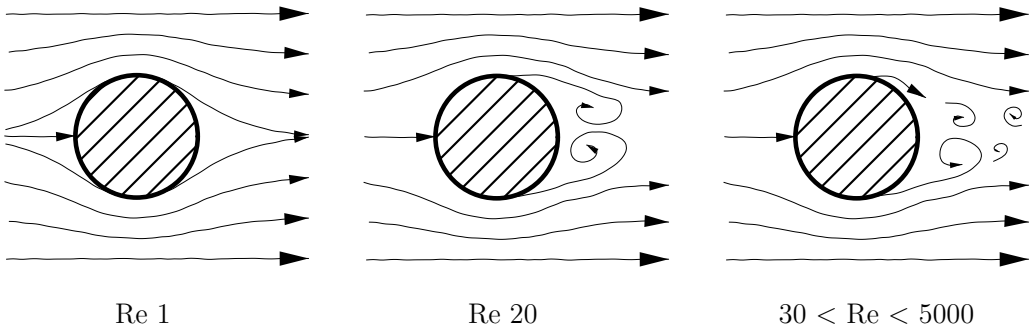

Figure 2.4: Flow pattern at different *Re* numbers

3

Wind loads on buildings

This chapter transitions from the fundamental fluid mechanics concepts introduced in Chapter 2 to their practical application in wind engineering. The focus shifts from understanding wind behavior itself, to how empirical design codes represent it for determining wind loads on buildings and structures.

3.1 The Atmospheric Boundary Layer (ABL)

In building engineering (or practically most engineering fields except aerospace), wind and subsequent wind loads refer to flows within the Atmospheric Boundary Layer (ABL). This layer of air stretches from the Earth's surface up to hundreds or thousands of meters, its depth and behavior varying with terrain roughness, topography, and current weather conditions (Simiu, 2019). A dominant characteristic of ABL winds are their turbulent nature, resulting in high variability. Due to this variability, wind loads cannot be deterministically known – wind loads are a inherently a function of probability.

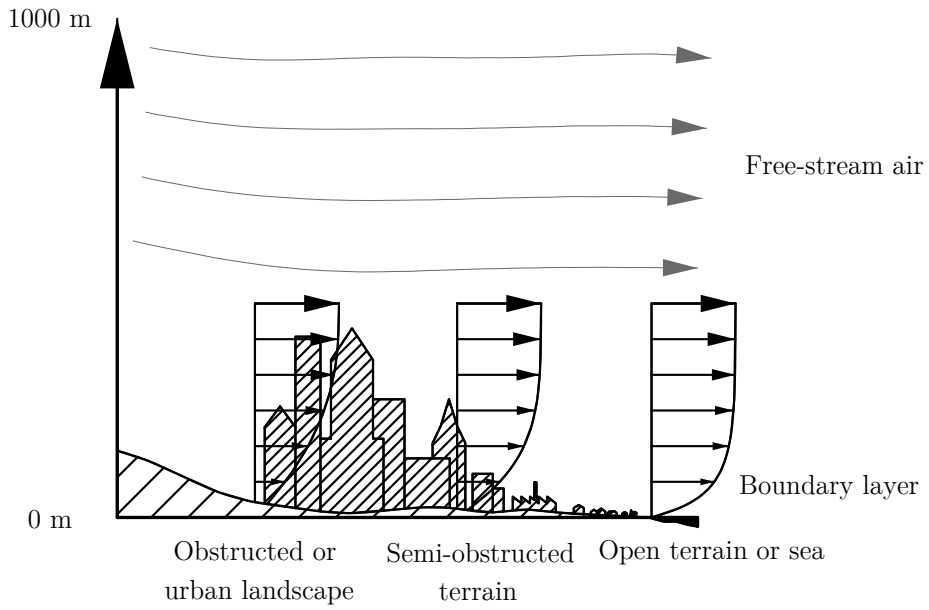

Figure 3.1: Typographies within the ABL and the formation of a boundary layer

3.1.1 Terrain and topography

Terrain has a significant influence on the formation of the ABL. Topographic roughness exerts friction on the wind, gradually slowing down its velocity to zero at the ground level (Simiu, 2019; An et al., 2023) and the extent of this effect depends on the aerodynamic roughness of the terrain. In Eurocode, the roughness length z_0 is used to quantify this effect, defined for five distinct categories according to Table 3.1.

Table 3.1: Terrain categories and parameters

	Terrain category	z_0 [m]	z_{min} [m]
0	Sea or coastal area exposed to the open sea	0.003	1
I	Lakes or flat and horizontal area with negligible vegetation and without obstacles	0.01	1
II	Area with low vegetation such as grass and isolated obstacles (trees, buildings) with separations of at least 20 obstacle heights	0.05	2
III	Area with regular cover of vegetation or buildings or with isolated obstacles with separations of maximum 20 obstacle heights (such as villages, suburban terrain, permanent forest)	0.3	5
IV	Area in which at least 15 % of the surface is covered with buildings and their average height exceeds 15 m	1.0	10

Major international codes often generally agree on the important categories, however there is not consensus on the exact numerical value of z_0. Furthermore, while most areas are covered by terrain categories, current studies emphasize the inability to account for highly local and specific conditions such as tall buildings and street configurations, that generate local wind conditions distinct from the ABL itself (An et al., 2023; Picozzi et al, 2023).

3.1.2 Mean velocity profiles

From having zero velocity near ground, the wind speeds gradually grow to the free-stream velocity in proportion to the diminishing influence of the surface roughness, measured in z_0. One well established, general representation of the velocity growth over height is the logarithmic profile, expressed as:

$$u(z) = \frac{u^*}{\kappa} \cdot \ln\left(\frac{z + z_0}{z_0}\right) \tag{3.1}$$

where the *friction velocity* u^* and the *von Karman constant* κ are:

$$u^* = \frac{\kappa \; u_{ref}}{\ln\left(\frac{z+z_0}{z_0}\right)} \tag{3.2}$$

$$\kappa \approx 0.4 \tag{3.3}$$

In Eurocode, mean wind speed v_m are in principle calculated using a logarithmic model, however not strictly presented as the general logarithmic model in Equation 3.1. Standard Eurocode include factors such as the roughness factor c_r multiplied by the site-dependent reference wind speed v_b, in contrast to the friction velocity u^*, as well as the orography factor c_o (influence of steep terrain conditions):

$$\begin{aligned} v_m &= v_b \cdot c_r(z) \cdot c_o \\ &= v_b \cdot k_r \cdot ln\left(\frac{z}{z_0}\right) \cdot c_o \\ &= v_b \cdot 0.19 \cdot \left(\frac{z_0}{z_{0,II}}\right)^{0.07} \cdot ln\left(\frac{z}{z_0}\right) \cdot c_o \end{aligned} \tag{3.4}$$

Current Eurocode determination of wind velocity has an upper limit in terms of applicability of 200 meters, which means that for taller structures, wind speeds cannot be predicted using Eurocode exclusively (EN-1991-1-4, 2005)

The logarithmic profile has a strong established empirical as well as theoretical basis (Holmes, 2015). However, not all major standards utilize the logarithmic profile, for example the Architectural Institute of Japan (AIJ) guidelines, Canadian and American code utilize the power law profile (Bashor et al., 2019). The power law wind velocity profile expressed in general terms is:

$$v = u_{ref} \cdot \left(\frac{z}{z_{ref}}\right)^{\alpha} \tag{3.5}$$

With a power law profile, roughness is rather expressed by the exponent α. Either model have been used to design reliable structures, but the fundamental difference (and the mathematical implications alone) results in a difference in predicted wind speeds between the models at certain heights.

3.1.3 Wind turbulence

As noted, a dominant feature of the winds in ABL are that they are turbulent, which in more practical terms means that the winds contain a fluctuating "gustiness" (Holmes, 2015) that periodically increase or decreases wind speeds. This variation of wind speeds has found to be effectively measured using the standard deviation:

$$\sigma_v = \sqrt{\frac{1}{T}\int_0^T (U(t) - \bar{U})^2 dt} \tag{3.6}$$

where $U(t)$ – the total velocity – is equal to $\bar{U} + u(t)$, where $u(t)$ is the fluctuating (turbulent) velocity in the wind direction. This has strong similarity to the Reynolds decomposition in Section 2.4: Equation 2.21.

The standard deviation of wind speeds has been found to be approximately equal to 2.5 times the friction velocity u^* (Holmes, 2015). With this, the *turbulence intensity* I_v can be expressed as:

$$I_v = \frac{2.5u^*}{(u^*/0.4)\ \ln(z/z_0)} = \frac{1}{\ln(z/z_0)} \tag{3.7}$$

This implies the turbulence intensity to be directly correlated to the height and surface roughness which also makes sense intuitively: the presence of rough terrain, physical objects and shear layers disturbs the flow – mainly at lower heights.

In Eurocode (EN-1991-1-4, 2005), turbulence intensity is for most purposes represented by Equation 3.7, however a small modification allows for the consideration of a *turbulence factor* k_I and the terrain orography c_o (which are normally equal to 1), as expressed in Eurocode:

$$I_v = \frac{\sigma_v}{v_m(z)} = \frac{k_I}{c_o(z) \cdot \ln(z/z_0)} \tag{3.8}$$

Conversely, turbulence intensity is expressed as a power law for the codes that are based on this (Holmes, 2015).

3.1.4 Probabilistic basis of design wind speeds

Due to the turbulence and the spread in wind speeds values, the expected occurrence of peak velocities is expressed by a probabilistic distribution (Holmes, 2015). Common measurement methods samples wind speeds over a period of time, often over 10 minutes, and expresses the probability of a peak *gust* wind speed $\hat{U}$ within this period as a function of the normal distribution σ_v and the *peak factor* g as:

$$\hat{U} = \bar{U} + g\ \sigma_u \tag{3.9}$$

The gust factor is the ratio between the maximum gust speeds and the mean wind speeds, expressed as:

$$G = \frac{\hat{U}}{\bar{U}} = \frac{\bar{U} + \sigma_v}{\bar{U}} = 1 + g\ I_v \tag{3.10}$$

In standard Eurocode, the gust factor is represented by the term $[1+7 \cdot I_v(z)]$, which appears in the calculation of peak pressures. There are however differences between National Annexes (adaptions) and the standard Eurocode method of determining the gust factor, where notably the Swedish annex uses:

$$G = [1 + 2 \cdot k_p \cdot I_v] \tag{3.11}$$

where k_p often is set to 3 for typical cases, unless the natural frequency of the building needs to be taken into account, such as for tall and slender building (EN-1991-1-4, 2005).

3.2 Static wind loads

The pressures from wind hitting the building and subsequent wind loads can for all major building codes principally be regarded as a function of velocity pressures q_b, the gust factor G and the pressure coefficient c_p, the latter also depending on the specific surface or shape which is studied. The general format of this function can be expressed by Equation 3.12:

$$q = q_b\ \cdot G\ \cdot c_p \tag{3.12}$$

However, beyond this very general format, many variations and differences exists between building codes and standards, particularly how the wind speeds and the gust factor are determined (Holmes, 2015). In standard Eurocode, peak surface pressures are calculated by:

$$q_p(z) = [1 + 7 \cdot I_v(z)] \cdot \frac{1}{2} \cdot \rho \cdot v_m^2(z) \tag{3.13}$$

This is then multiplied by pressure coefficient c_{10} or c_{p1} which are tabulated, predetermined, values strictly related to the studied typology (e.g walls, roof), wind direction and size (10 meter element or 1 meter element for smaller/detailed checks).

3.3 Dynamic wind loads

In general terms, the transient gust component of winds give rise to accelerations, which creates a dynamic response of the building. If the natural frequency of a building is sufficiently low (typically less than 1 Hz) and its *damping* (aerodynamic or structural), is not sufficiently high, the periodic characteristics of wind can excite a resonant response of the structure, where slender and flexible structures are particularly sensitive. Furthermore, the specific resonance *mode* can have a large significance for building design. Torsional modes, for instance, are generally considered especially challenging to treat (Holmes, 2015).

3.3.1 Aerodynamic effects

Beyond the intrinsic fluctuating component of wind and the subsequent dynamic response, the aerodynamic interaction between the wind flow and the building shape can also generate dynamic loads. Though distinct in their mechanism, they are here summarized as the aerodynamic effects (Sadeghi, 2021):

- **Vortex shedding**: involves periodic shedding of vortices, which generates an oscillating pressure difference between the cross-wind sides of a structure.
- **Galloping**: characterized by large-amplitude, low-frequency oscillations typically in 1 degree-of-freedom, which creates a relatively simple vibration shape.
- **Flutter**: typically involves higher frequencies and a stronger connection between the shape, aerodynamic response and oscillation modes, as well as more complex modes in contrast to galloping. The previously mentioned Tacoma Narrows Bridge collapse was a case of flutter.

4

Computational Wind Engineering

Although the expressions and descriptions of fluid behavior in Chapter 2 appears to naturally extend to numerical solutions of the mathematical equations via Computational Fluid Dynamics (CFD), the necessary and complex adaptations – going from continuous equation to discrete forms – fundamentally influences the outcome of the solution. This is a critical drawback of numerical methods (Simiu, 2019) and consequently, though they are expensive and cumbersome, physical wind tunnel tests are still the dominant benchmark for producing tailored wind effect predictions.

Computational Wind Engineering (CWE) is a distinct subset of the CFD field, focusing on predicting and simulating wind for the built environment (Simiu, 2019). Despite the inherent issues of the discretization required for CFD, there are numerous potential application that are continuously being explored with promising results, including but not limited to; prediction of pedestrian wind speeds, natural ventilation, architectural shape optimization, HVAC design, complex terrain flows and dispersion (Blocken, 2014; Cochran et al., 2011; Stathopoulos, 1997; Thordal et al., 2019).

No less, CWE is also being recognized in the currently drafted second generation of Eurocode, as seen in prEN 1991-1-4:2021 (Hansen et al., 2019; Ricciardelli, 2023), and is already present in Architectural Institute of Japan (AIJ) codes (Tamura et al., 2008). Despite this, widespread adoption in structural engineering is limited, mainly due to the generally high complexity of CFD and the perceived trustworthiness of the simulation. A failure to determine sufficient wind loads due to improper simulation is potentially disastrous while setting up a CFD simulation requires many consequential choices, beyond the inherent challenge of discretization.

Evident by the ongoing research, the potential is still large and the recognition of CWE in Eurocode points to this. Future developments, while neither replacing empirical codes or wind tunnel test, could assist in early design, and broadly give guidance when treating complex typologies, contexts, terrain and climatic conditions, compared to the inherently limited design codes and standards.

This chapter will firstly focus on CFD in general in Section 4.1, then the current landscape of CWE and structural design in Section 4.2.

4.1 Numerical simulation and CFD

Essentially, the CFD simulations in CWE operate on similar principles to physical wind tunnel on a surface level; a building is placed centrally in a testing (simulation) domain, with assigned wind inlet and outlet (boundary) conditions that direct wind flow across the domain, interacting with the building. However, there are many specific and crucial differences of CFD in contrast to wind tunnel testing.

4.1.1 Discretization of the governing equations

The Navier-Stokes equations are the fundamental governing equations that are numerically solved during a CFD simulation (Simiu, 2019). As presented in Section 2.1.3, the Navier-Stokes equations consist of a conservation of mass statement for an incompressible fluid (1), and a conservation of momentum statement (2):

$$\begin{aligned} \text{(1) Mass conservation:} \quad & \nabla \cdot \vec{u} = 0 \\ \text{(2) Momentum conservation:} \quad & \rho \left(\frac{\partial \vec{u}}{\partial t} + \vec{u} \cdot \nabla \vec{u} \right) = -\nabla p + \mu \nabla^2 \vec{u} + \vec{f} \end{aligned} \tag{4.1}$$

Furthermore, as previously noted the Navier-Stokes equations are infamously complex which, in short, necessitates an iterative and discretized solution. The discretization refers to both the discretization of the equations, and the spatial discretization of the domain into subdomains (mesh) in which the calculations are iteratively solved.

The most well-established method of discretization is the Finite Volume Method, FVM (Simiu, 2019), together with the SIMPLE (Semi-Implicit Method for Pressure-Linked Equations) algorithm approach, or a variation of the SIMPLE algorithm (CFD Online, 2016). The steps of the SIMPLE algorithm are in a condensed manner described below:

1. Boundary conditions are set, normally Dirichlet boundary conditions: velocity assigned at inlet, pressure assigned as zero at outlet.
2. The momentum equation (2) is approximated with an initial pressure field guess.
3. Approximated pressure field is then corrected with the mass conservation (1).
4. The corrected pressure field is applied to a previously approximated velocity field to obtain a new velocity field.
5. Iterative steps until the mass conservation (1) and the momentum conservation (2) are both satisfied.

4.1.2 Turbulence treatment

As noted in Section 2.4, turbulence consists of "swirling eddies superimposed at many different temporal and physical scales". At the overall physical dimensions of a building, the turbulent structures could cover a massive range in scales: from the size of a building (hundreds of meters) down to the dissipative *Kolmogorov* scales (0.1 mm), where the fluid can absorb the turbulent energy (George, 2013). This scale disparity makes data and computation requirements (literally) impossibly large.

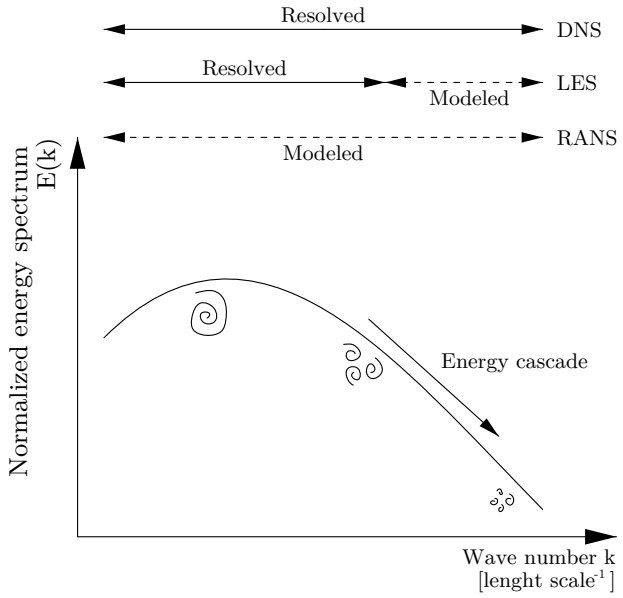

Figure 4.1: Turbulence spectrum

Nearly all practical CFD applications therefore employs mathematical models for turbulence, in order to capture the relevant impact of turbulence without *resolving* it fully (Simiu, 2019). In contrast however to using turbulence models, **Direct Numerical Solution** does resolves all scales of turbulence, which can give highly representative results of real life fluid behavior, but suffer from the massive computation cost in atmospheric flows (high Re numbers).

Large-Eddy Simulation (LES) is a transient approach that resolves larger turbulent scales, while employing a representative model for smaller scales, making it a more moderate approach than DNS since not all scales of turbulence is resolved. This means that the grid size only needs to be small enough to capture the behavior of the relevant eddies.

Reynolds-Average Navier-Stokes (RANS) is one of the most widely applied turbulence representation as it runs fast and reliably in comparison, however resulting in a steady-state result. RANS employs a model to represent all scales of turbulence, which is done based on the Reynolds decomposition (Equation 2.21), assuming wind velocity consists of a mean and a fluctuating component expressed in Equation 4.2:

$$u(x,t) = \overline{u}(x) + u'(x,t) \tag{4.2}$$

Replacing the velocity in Navier-Stokes equations with two expressions for mean and fluctuating velocities yields an unknown variable; Reynold's Stresses (Andersson, 2024) which needs additional treatment, called the closure problem (of the Navier Stokes equations). The closure problem can be treated by several assumptions of the representation of these stresses, and ways to link them with the overall fluid properties, called *turbulence models* (Simiu, 2019)

Three commonly used RANS turbulence models are $k-\epsilon$ model, $k-\omega$ model and $k-\omega$ SST model; all based on one equation to capture the turbulence kinematic energy k, and an additional equation to capture either turbulence dissipation rate ϵ or the specific turbulent dissipation rate ω:

- The $k-\epsilon$ model captures free stream flows with good accuracy, but is less capable of resolving flow with sharp gradients which occur near walls and flow separation of bluff bodies.
- The $k-\omega$ model is better suited at low Re numbers, where the viscous effects are stronger i.e near walls.
- The $k-\omega$ SST model combines both, and attempts to utilize the strengths of the $k-\epsilon$ model in free flows and the strengths of the $k-\omega$ model near walls

4.2 Current CWE practice

This section sets the stage for current CWE practice and relates key factors of the broader context of CWE and structural design with the aims of this thesis, including the usage of IBOFlow.

4.2.1 Meshing and modeling

Typical CFD solvers are based on a Finite Volume Method discretization, and the generated mesh is generally body-fitted to the building which means that it stays as close to the building shape as possible. The meshing level of detail has a large importance for capturing critical and detailed areas of the wind flow such as boundary layers and turbulent structures (Franke et al., 2007). Additionally, the *quality* of the mesh is important, which is why the meshing itself demands high expertise of someone who knows what a 'high quality mesh' implies, which generally reduces accessibility of CWE methods for structural engineers.

The overall dimensions of the simulation domain has an impact on capturing proper terrain boundary layers and developing the flow around the building. Consequently, common practice is to set a distance related to the building height H, from the building to the inlet, outlet and side boundaries. Inlet distances range from 2H to 5H, while outlet distances are more, up to 15H, to allow the flow to fully develop. Vertical and lateral extensions are often set to around 4H and 2.5H respectively, typically depending on the percentage of *blockage* (Franke et al., 2007). The blocking effect refers to the tendency of the flow accelerating when significantly obstructed, and must be minimized.

4.2.2 Inlet conditions

The inlet conditions can vary, but it is common for RANS based simulations to use the logarithmic profile with atmospheric boundary layer mean wind speeds, meaning that they gradually increase from a low value near the terrain, as shown in Equation 4.3:

$$u = \frac{u^*}{\kappa} \ln\left(\frac{z + z_0}{z_0}\right) \tag{4.3}$$

The turbulent component is also assigned at the inlet through assigning the turbulence kinematic energy k as shown in Section 4.1.2. Three different ways to calculate k for the inlete are presented here, firstly one based on the turbulence intensity I:

$$k_I = \alpha \cdot (I \cdot u)^2 \tag{4.4}$$

where α can be chosen as 1 (Tominaga et al., 2008), I is the turbulence intensity and u is the wind velocity.

The turbulence intensity I can either be measured (for instance when comparing to a wind tunnel test) or calculated through established code, for instance Equation 3.7. If the velocity u follows an logarithmic function and I follows an *inverse* logarithmic function of height respectively (as in Eurocode), then the product is constant. This produces the second representation of turbulent kinematic energy k in Equation 4.5:

$$k_{ABL} = \frac{(u^*)^2}{\sqrt{C_\mu}} \tag{4.5}$$

where $C_\mu = 0.09$ (SimScale, 2024). A variation of this is that if measured data on the turbulent intensity I is known, a curve fit routine could be performed in order to better capture the specific conditions, producing the final representation of turbulent kinematic energy k in Equation 4.6

$$k_{model} = \frac{(u^*)^2}{\sqrt{C_\mu}} \cdot \sqrt{C_1 \ln \frac{z - z_0}{z_0} + C_2} \tag{4.6}$$

where the C_1 and C_2 in the square product are used to calibrate the model (SimScale, 2024).

4.2.3 Validation, verification and error

To verify the credibility of results, two aspects are crucial: verifying the simulation functions as expected (on a technical basis; fluid flows from inlet, interacts with subject etc.) and validating that the results are physically representative of reality. In practice, validation requires comparison to wind tunnel tests or other empirical data, either through previous research or a parallel test. Without validation, a "solved" simulation cannot be assumed to produce useful results.

The technical verification relies on monitoring convergence during iterative solving. As the simulation solves the equations, it produces a residual that quantifies numerical error. Guidelines recommend minimizing this to at least 1×10^{-4} (Franke et al., 2007), though this threshold has neither been widely accepted nor proven universally applicable, with alternative values proposed (Mitkov et al., 2024). Importantly, a minimized residual confirms numerical convergence but does not guarantee physically relevant results, reinforcing why validation against empirical data remains essential.

4.2.4 Guidelines

To date, the most comprehensive guidelines for CWE applied to structural engineering are those presented by the Architecture Institute of Japan (Tominaga et al., 2008; Tamura et al. 2008), which provide instructions for LES simulation of facade pressures and RANS simulation of global forces. Many studies highlight RANS inadequacies and that its steady-state results fail to capture peak winds, the primary concern for structural engineers. However, AIJ codes treat steady-state, averaged RANS results as representative of the mean wind conditions already present in most codes, then apply gust effects to these results.

Eurocode references numerical simulation but does not yet provide implementation recommendations. The draft second-generation Eurocode, prEN 1991-1-4, includes Annex K with general CFD analysis recommendations aimed at helping practitioners commission analyses and understand design parameters (Hansen et al., 2019; Ricciardelli, 2023).

COST 732 (Franke et al., 2007) provides a clear summary of common recommendations but emphasizes pedestrian wind comfort studies rather than structural applications.

Lastly, all existing guidelines focus primarily on the conventional combination of RANS, FVM, and body-fitted meshes.

4.3 IBOFlow

There are many frameworks for CFD simulation, such as OpenFOAM, SimScale, ANSYS Fluent, STAR CCM+, to mention a few. Besides the complexity of any CFD simulation, outlined in previous chapters, another challenge of adoption is the software itself. They are often run on High Performance Computing (HPC) clusters after a rigorous setup and elaborate meshing routine.

In this context, the continued part of this thesis will investigate the usage and potential benefits of **IBOFlow**, a CFD solver developed by Fraunhofer-Chalmers Center (FCC), in a structural design context to elaborate on the future of CFD tools in structural design.

IBOFlow utilizes the Immersed Boundary (IB) method with a regular grid discretization over the domain (IBOFlow, 2025). In IBOFlow, the domain is discretized into a computationally efficient regular Cartesian Octree grid mesh. The studied objects boundary definition is *immersed* into the mesh and the individual cells of the mesh are categorized as either exterior (fluid) cells, boundary cells or interior cells. Due to the regular Octree grid structure, it also allows for a straightforward grid refinement routine around objects or other boundaries such as the ground and terrain, which can be done automatically in IBOFlow (IBOFlow, 2025).

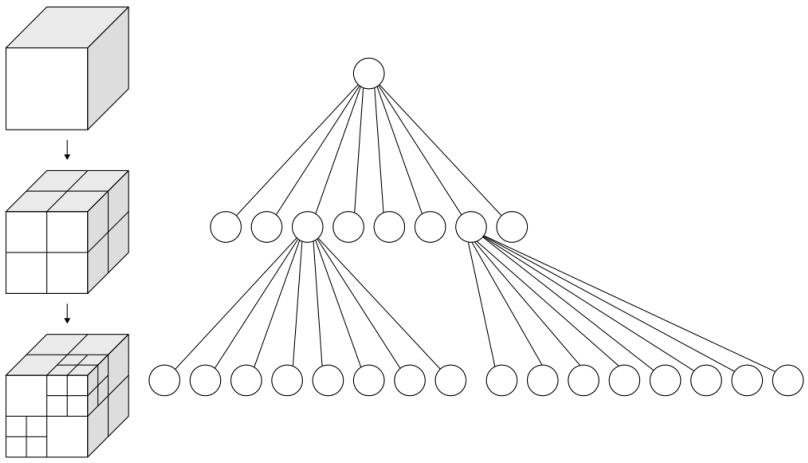

Figure 4.2: Octree grid and data structure

A key features of an Immersed Boundary Octree flow solver is that it makes meshing easier, and suitable when meshing is difficult either due to the complexity of geometry, or due to the expertise of the user. A conventional meshing routine often involves an irregular body-fitted meshing algorithm and deliberate configuration of refinement parameters around objects, often necessitating a more involved mesh convergence study.

Another benefit is the parallelization support; simulations scales well on GPUs (Graphical Processing Units), as well as consumer GPUs. They have many thousands of cores which can

offer a benefit in terms of runtime on "normal" hardware as opposed to large HPC clusters.

Specifically to IBOFlow, the *Mirroring* Immersed Boundary Method is utilized. In short, this is a specific contribution made by FCC (Mark et al. 2011), that utilize a reflective symmetry over the immersed boundary, which better captures the specific shape underneath despite the inexact discretization inherent to the Immersed Boundary method.

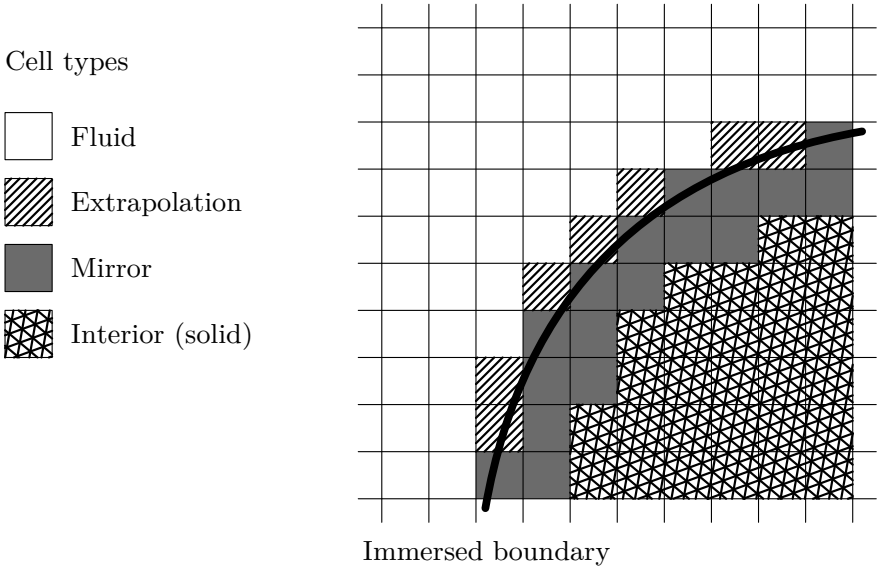

Figure 4.3: Cell types in Mirrored Immeresed Boundary

5

Validation of IBOFlow

IBOFlow has been used primarily for industrial and mechanical applications, but recent work by Vanky et al. (2023) demonstrated and extended its capabilities to urban wind flow simulation. Vanky et al. also evaluated IBOFlow's inherent benefits in terms of user friendliness and performance, fundamentally stemming from its meshing routine.

While urban wind flow relates to the built environment, IBOFlow has not yet been studied specifically for structural design applications, unlike many established FVM and body-fitted simulation methods. The benefits identified by Vanky et al. – user friendliness and performance – remains equally relevant for structural applications and are central to integrated, early-stage CFD analysis.

The validation of this chapter is based on Montazeri et al. (2012), who used a RANS-based approach to predict pressure coefficients on building facades and overall wind behavior around singular buildings. The resulting pressure coefficient c_p values can directly link CFD and lateral wind loads, which ultimately could inform key wind-related design choices.

Montazeri et al. investigated a singular medium-rise building, benchmarking numerical results against experimental wind tunnel data. The original wind tunnel experiment, assumed to reflect real-life values, served as the validation measure for the CFD simulation. Overall agreement in c_p-values and behavior was observed, with some important deviation primarily in presumed turbulent and negative pressure regions (i.e., the back of the studied building).

Montazeri et al. used conventional body-fitted FVM meshing rather than an Immersed Boundary method. Since the Immersed Boundary method has less verification and overall adoption compared to near-ubiquitous body-fitted FVM meshing routines, it is relevant to validate IBOFlow's accuracy in this context, done by replicating parts of Montazeri et al.'s study and comparing results to the original wind tunnel measurements.

5.1 Case description

The original wind tunnel study examined a building at 1:30 scale, with full scale dimensions of $18 \times 7.5 \times 15$ ($0.60 \times 0.25 \times 0.50$ meters at model scale). This was replicated in both Montazeri et al.'s CFD study and here using IBOFlow.

Inlet wind velocity was measured in the original wind tunnel experiment of $U_{ref} = 7.1\ m/s$ at the building height, along with turbulent intensity I, ranging from 3% to 13%.

5.1.1 Domain and boundary conditions

The simulation domain is a box with dimensions of $10.6 \times 10.25 \times 3$ meters. Inlet and outlet conditions are assigned on opposing sides: the inlet as a velocity inlet and the outlet as a pressure outlet with $p = 0$. The remaining walls are symmetry walls, setting normal velocity to zero and allowing non-zero tangential velocity.

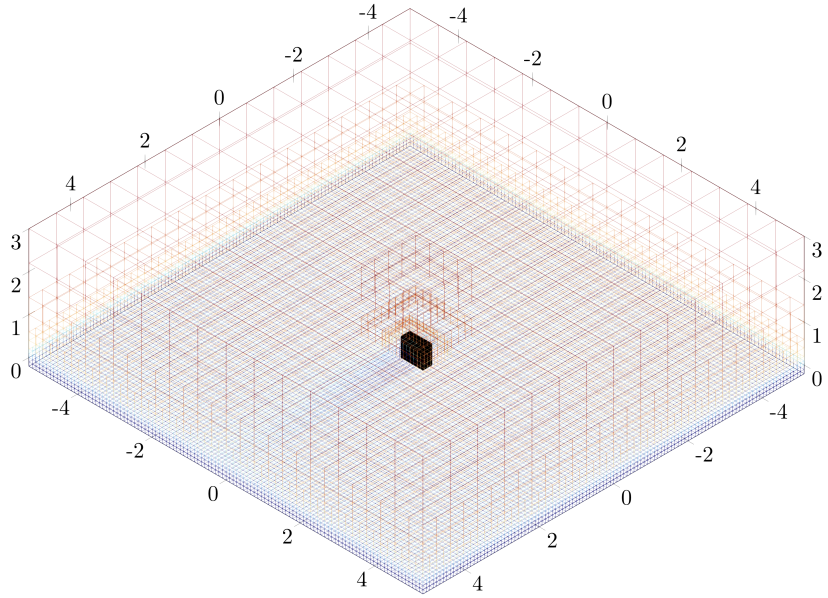

Figure 5.1: Virtual wind tunnel setup image; inlet at the top right; outlet at bottom left.

The assigned wind velocities at the inlet are modeled following a logarithmic profile curved describing the distribution of velocities across the height z, calculated by:

$$u = \frac{u^*}{\kappa} \ln\left(\frac{z + z_0}{z_0}\right) \tag{5.1}$$

where: $z_0 = 0.008$, $\kappa = 0.40$ and the friction velocity u^* was determined to be 0.73.

In Montazeri et al., the kinematic turbulent energy was measured across the height. To investigate a suitable way to represent these measurements, four methods to assign turbulent kinematic energy at the inlet from Section 4.2.2 are implemented and tested separately:

$$1: \quad k_{ABL} = \frac{(u^*)^2}{\sqrt{C_\mu}} \tag{5.2}$$

$$2: \quad k_{model} = \frac{(u^*)^2}{\sqrt{C_\mu}} \cdot \sqrt{C_1 \ln \frac{z - z_0}{z_0} + C_2} \tag{5.3}$$

$$3: \quad k_I = \alpha \cdot (\ I(z) \cdot u(z)\ )^2 \tag{5.4}$$

$$4: \quad k_{I-constant} = \alpha \cdot (I_{constant} \cdot u(z)\ )^2 \tag{5.5}$$

Although less calibrated for the specific case setup, evaluating the validity of the semi-empirical models (k_{ABL} or k_I) is important as they represent one of few alternatives when

the required data for curve fitting (k_{model}) is unavailable.

Lastly, the turbulence model $k-g$ SST is used; an equivalent to the $k-\omega$ SST model (Section 4.1.2) but formulated for the Immersed Boundary method.

5.1.2 Mesh parameters

For a mesh sensitivity study, three levels of grid refinement was simulated denoted as G1, G2 and G4. The domain is divided into cells according to Table 5.1 for each of the principle axis of the domain. Afterwards, a local refinement routine close to the building was performed to further subdivide the cells in up to 4 steps.

Table 5.1: Grid configurations and cell counts

Level	X	Y	Z	X×Y×Z	Active Cells	Total Cells
G1	7	7	2	98	46424	58968
G2	14	14	4	784	289816	440776
G4	28	28	8	6272	1624628	3033464

To illustrate the increase in amount of cells, Figure 5.2 shows a bar plot for each refinement level and the roughly quadruple increase of active cells for each refinement level.

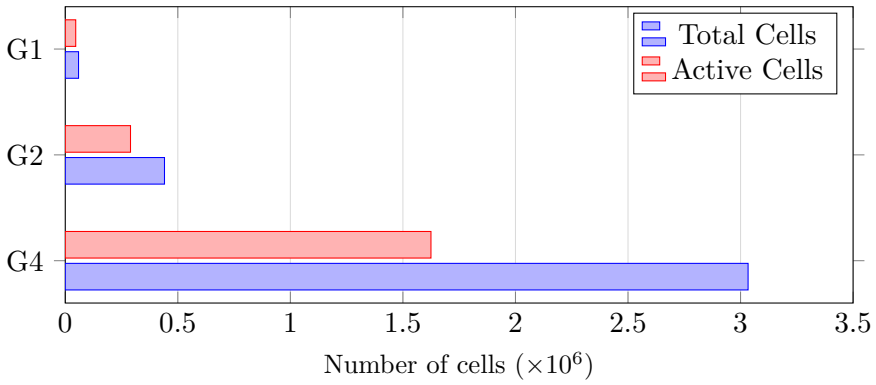

Figure 5.2: Comparison of Active and Total Cells for Grid Levels G1, G2, and G4

A notable feature is that as global refinement increases, the total amount cells grows non-linearly in relation to the active cells due to the local refinement routine occurring within the solid material. Cells not denoted as active, i.e cells within the solid material does not have an influence on the results.

The grid resolution needs to be sufficiently detailed to capture the velocity and turbulent kinetic energy profiles at the inlet. It also needs to be sufficiently detailed to capture relevant aerodynamic effects such as the formation of boundary layers and adverse pressure gradients, affecting the building and the predicted c_p value.

5.1.3 Residual parameter

Three different residual limits were tested to explore the results' sensitivity to residuals: 1×10^{-4}, 1×10^{-5}, and 1×10^{-6}. The residual parameter largely controls how long the simulation runs. While longer simulation time allows more time for aerodynamic structures to form

and presumably yields more qualitatively representative results, it does not automatically produce values closer to the wind tunnel data, as discussed in Section 4.2.3.

5.2 Results of validation

In the original experiment, the validation metric was primarily the pressure coefficient c_p, measured along four distinct location as illustrated in Figure 5.3. Obtaining pressure coefficient values that are overall physically consistent with reality is fundamental if the method is to offer an useful alternative to code or wind tunnel experiment. In all graphs, Position 1 – 4 respectively corresponds to the locations in Figure 5.3.

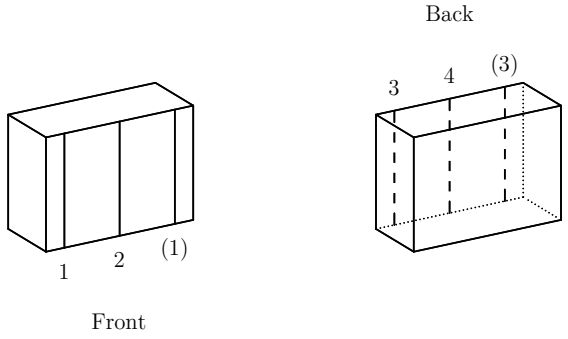

Figure 5.3: Sample positions

In summary, an inlet model study, mesh refinement study, and a residual convergence study was performed along with runtime performance measurements. The verification of the parameters in each study aims to provide a basis of how to operate IBOFlow, while the best-case results are compared to the original wind tunnel data in order to validate the method.

5.2.1 Inlet turbulence model

Inlet turbulence was modeled with four different approaches: two relying on semi-empirical data about atmospheric turbulence (k_{ABL}, $k_{I-constant}$) and two based on extracting the original wind tunnel experiment data (k_I, k_{model}). In Figure 5.4, the four different inlet models are compared. For each inlet model, the G4 grid scaling as well as a maximum residual of 1×10^{-5} was used.

The error, or deviation from the wind tunnel data, is summarized in Table 5.2 and 5.3. "Absolute error" refers to the mean of absolute errors for all data points. "Mean error" is the mean of signed errors (positive and negative) for all data points. Practically, absolute error could represent the accuracy at specific facade locations, while mean error could represent the overall accuracy for the entire building (relevant when considering total forces on the foundation).

Table 5.2: Inlet model absolute error in %

Parameter	Position 1	Position 2	Position 3	Position 4	Average
k_{ABL}	10.4	17.1	4.2	5.6	9.3
k_I	6.2	8.6	21.8	10.9	11.8
k_{model}	6.1	8.3	21.8	10.4	11.6
$k_{I-constant}$	9.9	14.9	3.7	4.8	8.3

Table 5.3: Inlet model mean error in %

Parameter	Position 1	Position 2	Position 3	Position 4	Average
k_{ABL}	6.8	16.8	3.8	4.0	7.8
k_I	3.6	4.4	21.8	10.9	10.1
k_{model}	3.9	3.7	21.8	10.4	9.9
$k_{I-constant}$	4.0	14.0	1.1	2.2	5.3

There is high similarity within the two sets of curve-fit and non curve-fit inlets respectively. The k_{ABL} inlet and the $k_{I-constant}$ inlet produce similar results, which correctly estimates the pressure values near the building height, while overestimating and diverging from the measured pressure coefficient at lower heights. However, the predicted values of the negative pressures behind the building are closer to the experiment values compared to the k_{model} inlet and the k_I inlet.

The k_{model} inlet and the k_I inlet are overall notably similar. In itself, this means that the curve fitting of the k_{model} inlet is an adequate representation of the raw data used in the k_I inlet. Each of them capture the pressure coefficients at the front accurately, but underperform at the back in the wake of the building where complex turbulent behavior and flow detachment can occur.

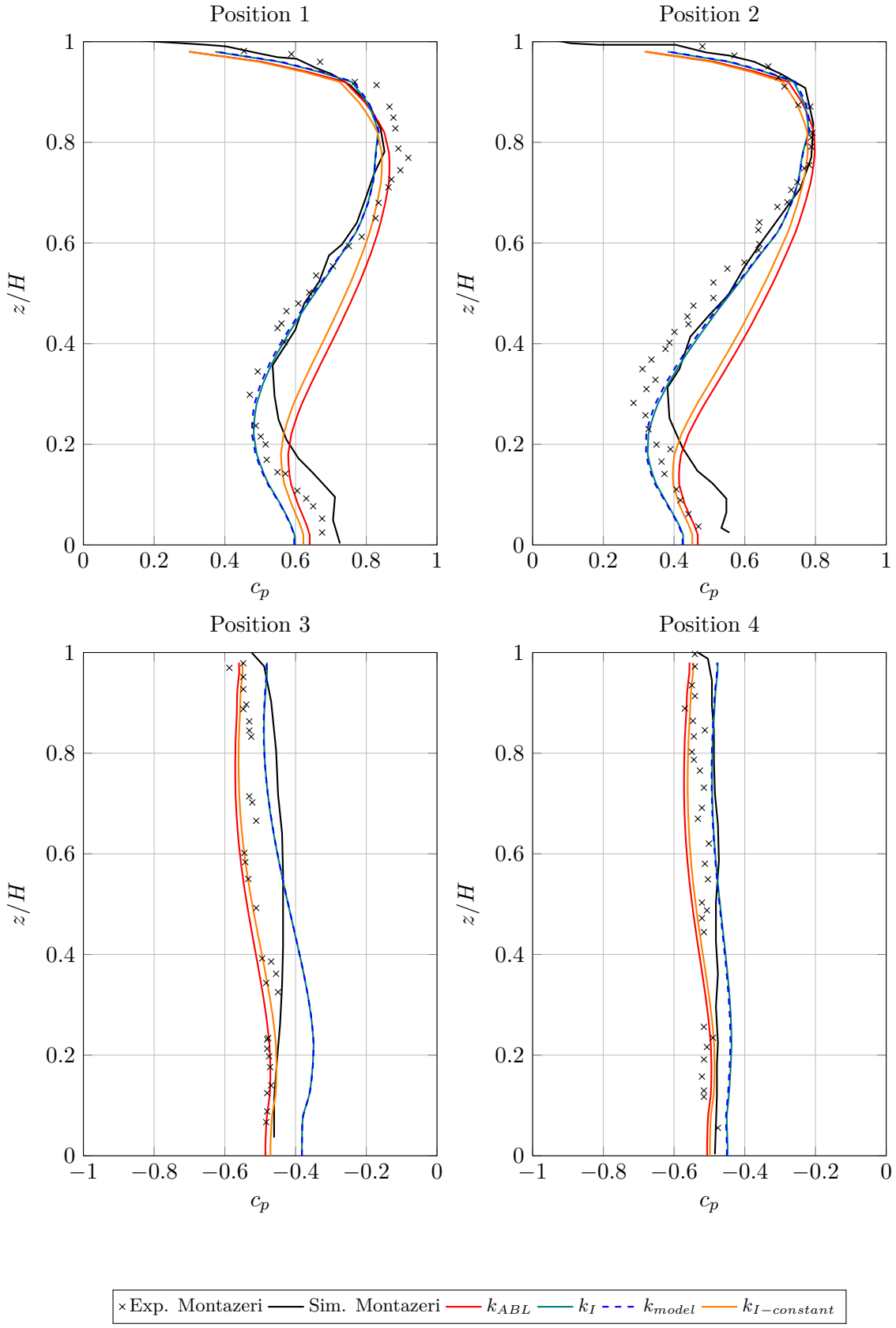

Figure 5.4: Inlet study: Profiles of c_p over z/H at each measurement position.

5.2.2 Mesh parameters

To evaluate the number of cells required to accurately represent the flow field around the building, a grid study was performed by scaling the base grid of $7 \times 7 \times 2$ cells. The scaling factors are denoted G1, G2 and G4, representing a 1, 2 and 4 factor scaling. Each simulation used the k_{model} inlet and 1×10^{-6} maximum residual.

Figure 5.5 presents the pressure coefficients c_p obtained at each sampling location. A qualitative evaluation of the pressure distributions shows that G1 produces noticeably coarse c_p results. This can also me seen in Figure 5.6. A more quantitative comparison in Figure 5.5 reveals that while G1 values do not always deviate significantly from the refined G2 and G4 meshes, the spatial resolution is insufficient to capture local peaks and small-scale variations in the flow field.

Interestingly, the coarser G1 resolution occasionally predicts pressures that align with experimental values, as revealed by Table 5.4 and Table 5.5, despite the courser flow structures. This should not be interpreted as validation of the courser mesh, but rather an indication that the numerical smoothing occurring at courser meshes may benefit some results; in this case the increased average negative pressure at Position 3 and 4, for a rectangular building.

Mesh resolution G4 shows generally good agreement between simulation and experimental c_p values, with an average error around 8-10%. At real-life scale, G4 divides the domain into base cells with real-life dimensions $W \times D \times H$ of $11.4 \times 10.3 \times 11.25$ meters, locally refined down to a minimum cell size of $0.71 \times 0.64 \times 0.70$ meters. The building at this scale has the dimensions of $18 \times 7.5 \times 15$ meters. The refined cell size is roughly 25 times smaller than the full building height, which could serve as a guideline for future IBOFlow application.

For geometrically complex buildings featuring balconies, facade variations or complex surrounding context, even higher global refinement levels than G4 may be necessary or increased local refinement, in order to correctly capture the intricate turbulent structures and flow phenomena.

Table 5.4: Mesh parameter absolute error in %

Parameter	Position 1	Position 2	Position 3	Position 4	Average
Grid G1	17.9	12.2	14.5	5.8	12.7
Grid G2	9.8	11.7	24.0	17.8	15.8
Grid G4	5.5	8.9	18.0	8.1	10.1

Table 5.5: Mesh parameter mean error in %

Parameter	Position 1	Position 2	Position 3	Position 4	Average
Grid G1	11.8	2.6	14.5	3.5	8.1
Grid G2	7.2	4.0	24.0	17.8	13.2
Grid G4	2.1	5.7	18.0	8.1	8.5

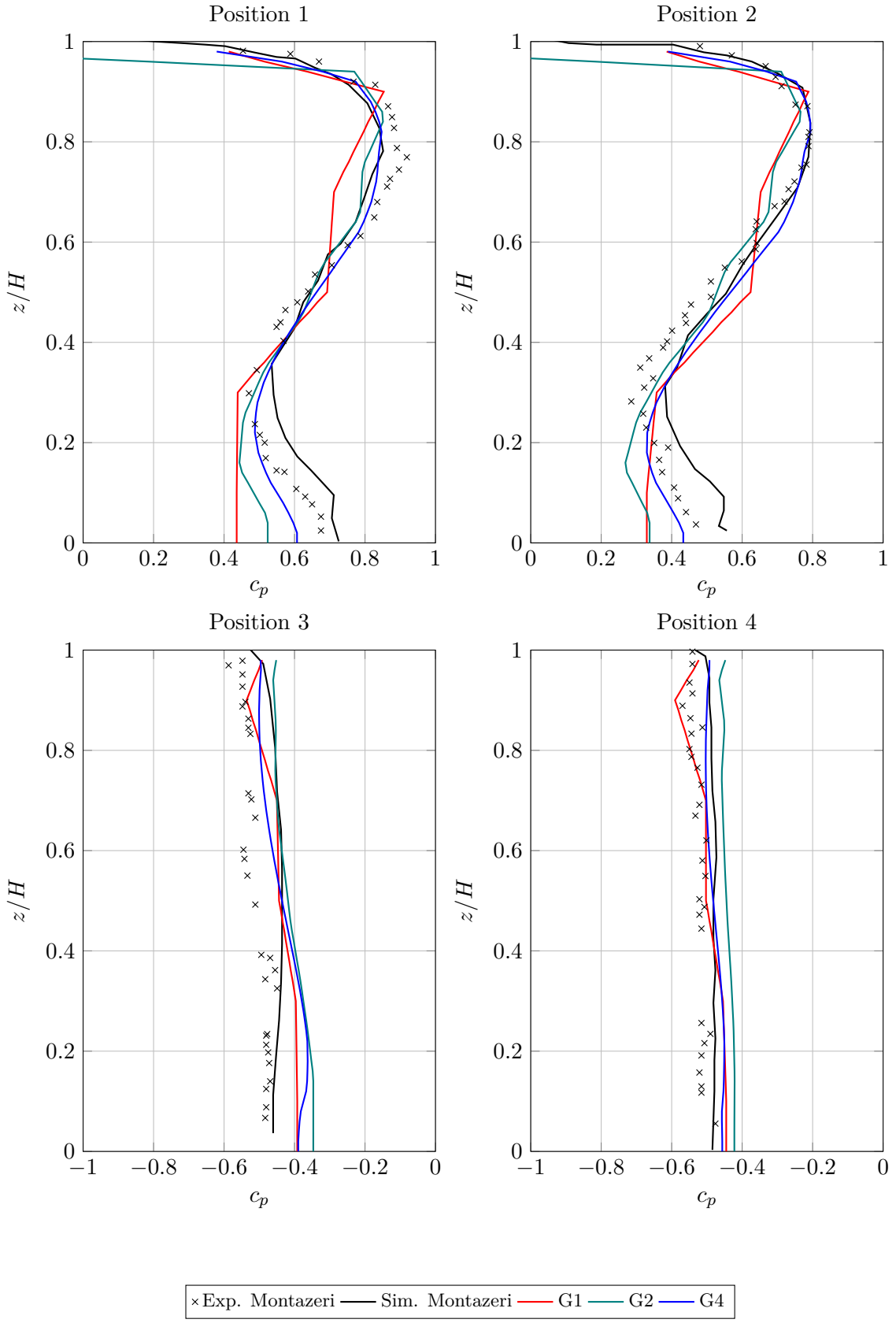

Figure 5.5: Grid study: Profiles of c_p over z/H at each measurement position.

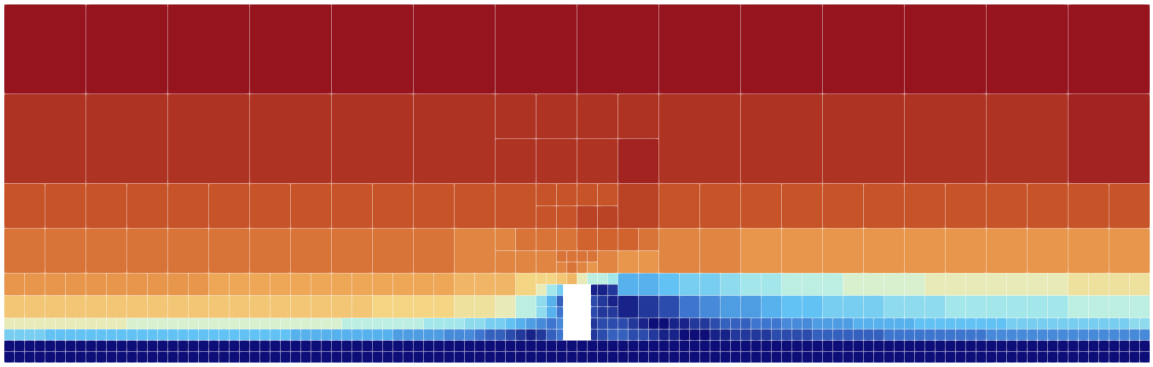

(a) G1 mesh

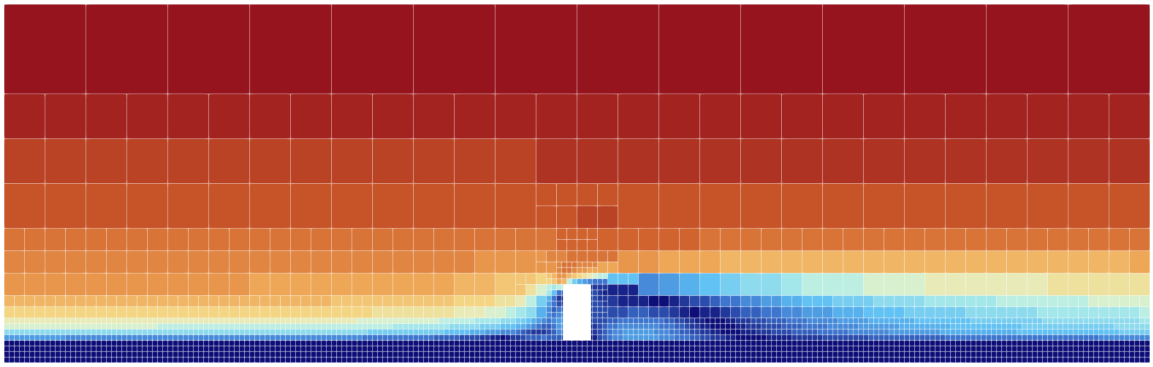

(b) G2 mesh

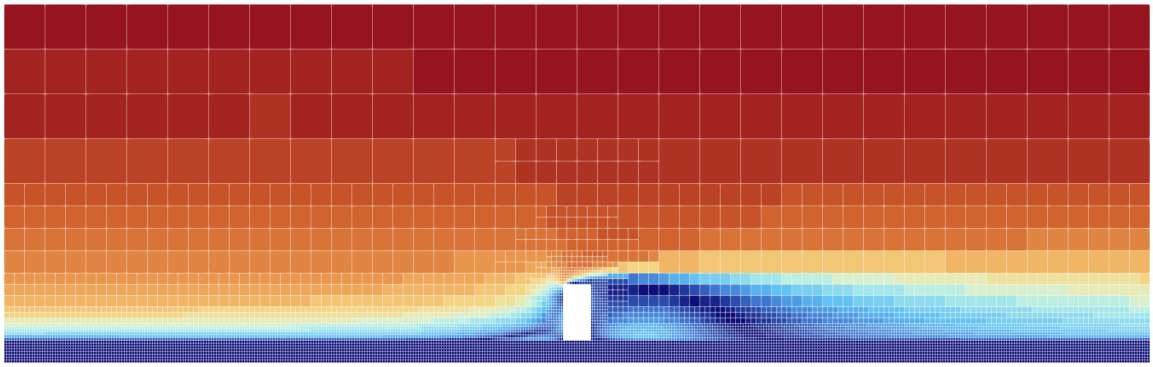

(c) G4 mesh

Figure 5.6: Illustration showing flow behavior at each grid refinement level

5.2.3 Residual parameter

To evaluate the iterative convergence behavior and its effect on the predicted pressure and velocity fields, the maximum residual threshold was set to 1×10^{-4}, 1×10^{-5} and 1×10^{-6}. When the threshold is reached, the simulation is terminated.

Minimal variation between 1×10^{-5} and 1×10^{-6} is observed, with both exhibiting similar predictions of the validation criterion c_p, as shown in Table 5.6 and Table 5.7. Both refined residual thresholds produce c_p values on the windward facade that closely match experimental measurements. In contrast, the coarser residual 1×10^{-4} generally underestimates windward pressures, indicating that the flow field has not yet fully developed before simulation termination.

Interestingly, at Positions 3 and 4 the residual 1×10^{-4} predict c_p values closer to wind tunnel data than the more converged 1×10^{-5} and 1×10^{-6} cases. This counter-intuitive result can be attributed to the incomplete development of the leeward flow field. The more refined residuals allow additional flow structures including turbulent structures and recirculation zones, which results in predicted negative pressures that underestimate the magnitude of negative pressure observed in wind tunnel experiments.

Results from both the grid convergence study and residual study suggest that flow solutions predicting greater wake separation, whether through higher resolution or through fully converged steady-state predictions, tend to underestimate leeward suction pressures compared to wind tunnel measurements. Predicted pressures in wake regions should be interpreted with appropriate caution.

Figure 5.7 shows that qualitatively, the results resemble overall aerodynamic behavior at any residual level.

Table 5.6: Residual parameter absolute error in %

Parameter	Position 1	Position 2	Position 3	Position 4	Average
Residual 1×10^{-4}	10.9	8.9	3.0	4.2	6.8
Residual 1×10^{-5}	6.1	8.3	21.8	10.4	11.6
Residual 1×10^{-6}	5.5	8.9	18.0	8.1	10.1

Table 5.7: Residual parameter mean error in %

Parameter	Position 1	Position 2	Position 3	Position 4	Average
Residual 1×10^{-4}	10.8	3.2	1.8	0.7	8.1
Residual 1×10^{-5}	3.9	3.7	21.8	10.4	9.9
Residual 1×10^{-6}	2.1	5.7	18.0	8.1	8.5

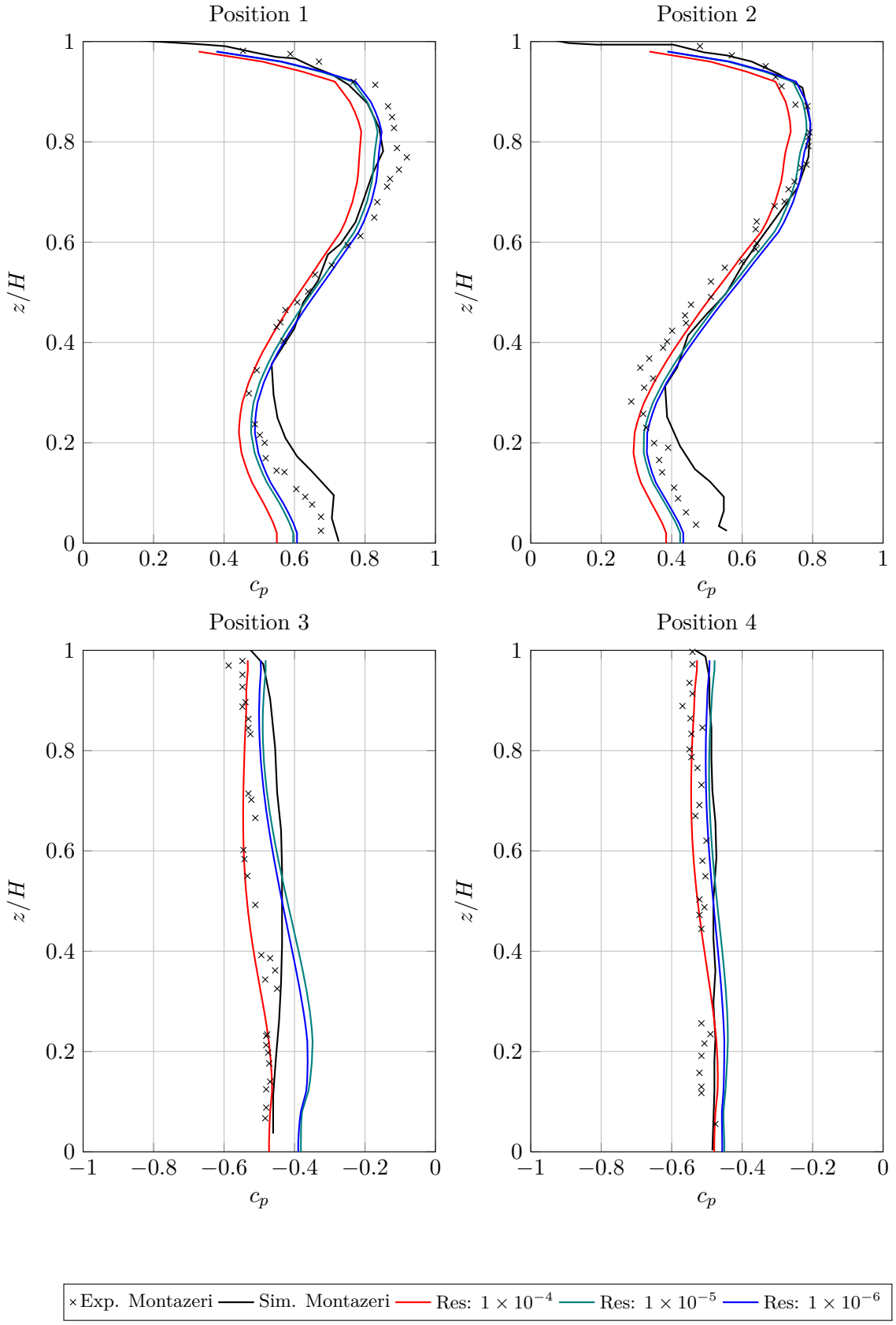

Figure 5.7: Residual study: Profiles of c_p over z/H at each measurement position.

5.2.4 Performance and runtime

All simulations were run on accessible, consumer-grade hardware with computing performance comparable to a standard office laptop (Table 5.8) in contrast to high-performance computing (HPC) resources which is otherwise common for CFD applications, due to the complex equations and necessary mesh resolutions. The accessibility theme of this thesis is closely linked to the simulation performance on accessible consumer hardware; whether CFD simulations has any practical relevance in early-stage structural design depends on the speed at which it can inform design decisions. In other words, if results requires several days to process, a CFD method might not be relevant, regardless of the accuracy.

Table 5.8: Computer hardware

Unit	Model
CPU	Intel Xeon W-10885M 8C 16T @ 2.40 GHz
RAM	2x16 GB DDR4 @ 2667 MHz
GPU	NVIDIA Quadro T2000 4 GB GDDR5 Max-Q

The computational performance of the iterative convergence study has been evaluated by comparing calculation times for residual thresholds 1.0×10^{-4}, 1.0×10^{-5}, and 1.0×10^{-6} using grid resolution G4. Table 5.9 shows that refining the residual threshold from 1.0×10^{-4} to 1.0×10^{-6} increases calculation time from approximately 40 to 90 minutes. Section 5.2.3 demonstrates that residual 1.0×10^{-4} produces generally unconverged results. Residual 1.0×10^{-5} could present an practical balance between overall accuracy and calculation times, reducing runtime by around 30% while achieving similar results for this specific case.

Table 5.9: Performance comparison of iterative convergence

Residual	1.0×10^{-4}	1.0×10^{-5}	1.0×10^{-6}
Active cells [n]	1.62×10^{6}	1.62×10^{6}	1.62×10^{6}
Iterations [n]	713	971	1356
Wall clock time [min]	40.6	66.2	94.3

The computational performance of the iterative convergence study was compared by the calculation times for the grid resolutions G1, G2 and G4.

The computational performance of the grid convergence study has been evaluated by comparing calculation times for grid resolutions G1, G2, and G4, all using a maximum residual threshold of 1.0×10^{-6}. As shown in Table 5.10, calculation time increases substantially with grid refinement from 2.2 minutes, to 12.9 minutes, to 90.1 minutes.

Notably, the computational efficiency measured as Active cells × Iterations/Second does not degrade exponentailly with refinement and in fact remains around 4×10^{-5} between refinement level G2 to G4. This favorable scaling suggests that the immersed boundary method maintains computational efficiency at higher resolutions, making refined grids practically accessible on consumer hardware.

Table 5.10: Performance comparison of grid convergence

Grid level	G1	G2	G4
Active cells [n]	0.046×10^6	0.29×10^6	1.62×10^6
Iterations [n]	591	1033	1356
Wall clock time [min]	2.2	12.9	90.1
Active cells × Iterations / Wall clock time [n/s]	2.1×10^5	3.9×10^5	4.1×10^5

5.3 Summary

A series of parametric studies was performed to validate IBOFlow and establish operational guidelines for structural design applications. The inlet boundary condition study demonstrated that inlet models based on curve-fitted or measured data (k_{model} and k_I) produce overall reasonable pressure distributions. Empirical inlet models (k_{ABL} and $k_{I-constant}$) show similar qualitative trends but with reduced quantitative accuracy, remaining useful when measured data is unavailable.

The grid convergence study revealed that mesh resolution represents a balance between accuracy and computational cost. While coarser resolutions (G1, G2) can provide qualitatively helpful predictions, their numerical values should be interpreted with caution. Grid resolution G4, with minimum cell sizes approximately 1/25 of the building height, achieved reasonable agreement with experimental data (8-10% average error) and is recommended as a baseline for simple rectangular buildings. More complex geometries may require additional refinement.

The iterative convergence study demonstrated that residual thresholds of 1×10^{-5} or 1×10^{-6} are necessary for converged solutions, with 1×10^{-4} producing unconverged results. Although the fully converged solutions underestimate leeward suction pressures compared to wind tunnel experiments, a known limitation of steady-state RANS for wake regions, achieving consistent, converged predictions is preferable to using accidentally accurate but unconverged results, as the latter provides no basis for systematic application.

Computational performance analysis showed favorable results. Calculation times ranged from 2 minutes (G1) to 90 minutes (G4 with 1×10^{-6}), with the recommended configuration (G4, 1×10^{-5}) requiring approximately 66 minutes on consumer-grade laptop hardware. The immersed boundary method demonstrated efficient scaling, making refined CFD simulations practically accessible for early-stage design iteration.

6
Case studies

Following validation, the IBOFlow method can be further demonstrated for practical wind flow analysis on buildings. While the validation in Chapter 5 revealed limitations of IBOFlow (particularly underestimated wake suction pressures) these do not discredit its usefulness for early-stage design. At this design phase, relative performance and qualitative flow behavior may be more valuable than exact numerical values. Comparative simulations indicating improvements between design alternatives can provide useful guidance for shape optimization, even if numerical results deviate from wind tunnel accuracy. Visualizations of flow patters can also inform code application where code-based methods are limited or ambiguous.

As established in the validation, predictions in wake regions require caution. The general recommendation is to use IBOFlow for comparative assessment and design guidance rather than as a substitute for code values or wind tunnel data, particularly when critical decisions depend on precise values in complex flow regions. With this approach, three case studies using IBOFlow along with a Rhino-Grasshopper integration are performed:

Case A: Mid-rise building and Eurocode provides a direct comparison between Eurocode and simulated wind forces for a mid-rise building. Furthermore, it examines the difference between the effect of blocking neighboring buildings, both estimated through Eurocode and simulation and the respective non-blocked predictions. Given that Swedish code notably prohibits this Eurocode method, wind loads might be overestimated when not considering blocking effects of neighboring buildings.

Case B: High-rise shape study explores tall buildings and several different geometric typologies. Eurocode is not valid for buildings above 200 meters and furthermore, the often varied and ambitious shapes of tall buildings makes predicting wind loads challenging without time-consuming wind tunnel studies, usually performed at later stages. Ideally, CFD simulations could assist predicting the impact of architectural design exploration on building aerodynamics; as well as its subsequent effect on structural design, at an early stage, provided the simulation is accurate.

Case C: Complex geometry and *Vertikal komposition* explores the impact on wind flow with the highly geometrically complex sculpture *Vertikal komposition*. The sculpture shape lacks any direct equivalence in Eurocode. Consequently, the structural engineers had to combine code usage with qualified assumptions and leading-edge empirical research. While significant focus was placed on the dynamic effects, the static surface pressure coefficients also presented a challenge, as well as the site terrain category. Dynamic effects are characteristically transient, in contrast to the capabilities of a steady-state CFD simulation, but it relies on several constants that can be related to the predicted flow field from CFD.

6.1 IBOFlow integration

The validation in Chapter 5 demonstrated that IBOFlow can produce results quickly, however, the setup itself can still be time-consuming. To facilitate and showcase the possibility of faster operations with IBOFlow was integrated into a common 3D CAD environment, namely Rhino+Grasshopper, by a collection of custom components scripted using Python language. The built-in components and robust geometry handling capabilities of Grasshopper are used to generate a triangular mesh representing the studied volume and surrounding. The general workflow is presented in Figure 6.1. The complete list of custom components written for the IBOFlow integration is detailed in Annex A.

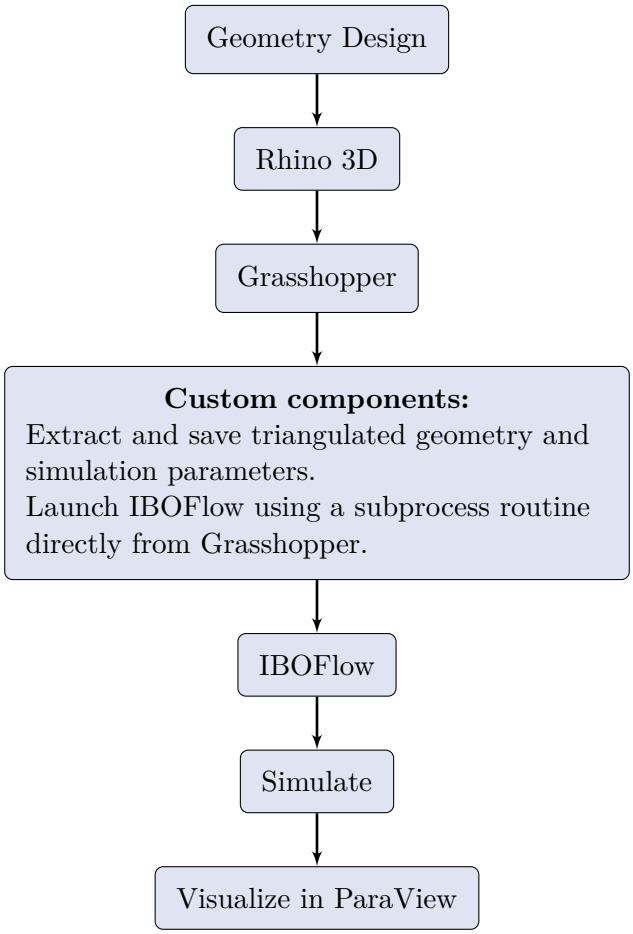

Figure 6.1: Geometry-to-simulation workflow using custom components.

6.1.1 Visualization of results

Visualization is performed using the external open-source software ParaView. ParaView is specifically developed for reading, processing, and exporting large-scale simulation datasets and offers extensive capabilities and versatility in post-processing CFD results.

6.2 Case A: Mid-rise building and Eurocode

A characteristic and simple mid-rise residential building of roughly 7 floors is calculated with an Eurocode approach to compare with resulting values from an IBOFlow CFD simulation. Firstly, the base velocity pressures are calculated with Eurocode based method and a CFD based method. Secondly, a study concerning neighboring buildings is performed. Standard Eurocode includes a procedure in Annex A.5 to take the impact of neighboring buildings on the wind speeds into account. Notably, following this procedure is not permitted in Swedish standards (Boverket, 2022), while simultaneously no directly equivalent alternative is provided.

6.2.1 Building parameters and wind pressures

The building footprint is 16 by 16 meters with a maximum height of 28 meters at the top of the roof, which has a 15 degree pitch. It is placed in a dense urban environment, equating to a terrain category IV by Eurocode classification (see Section 3.1.1).

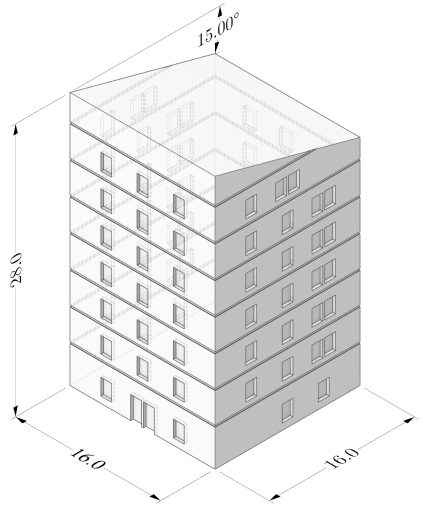

Figure 6.2: Measurements of the mid-rise building

Since the footprint width is smaller than the height, the velocity pressure is divided into one value for the bottom 16 meters and one for the remaining top 12 meters in accordance to Eurocode. This influences the roughness factor c_r, calculated through:

$$c_r = \begin{cases} k_r \cdot \ln\left(\dfrac{z_{bottom}}{z_0}\right) \approx 0.65 & \text{for } z = 16 \\ k_r \cdot \ln\left(\dfrac{z_{top}}{z_0}\right) \approx 0.78 & \text{for } z = 28 \end{cases} \tag{6.1}$$

where the terrain roughness factor $k_r \approx 0.23$. One wind speed for the bottom part and one for the top part is obtained:

$$v_m = \begin{cases} c_r \cdot c_o \cdot v_b \approx 16.9 \ \ m/s & \text{for } z = 16 \ m \\ c_r \cdot c_o \cdot v_b \approx 20.3 \ \ m/s & \text{for } z = 28 \ m \end{cases} \tag{6.2}$$

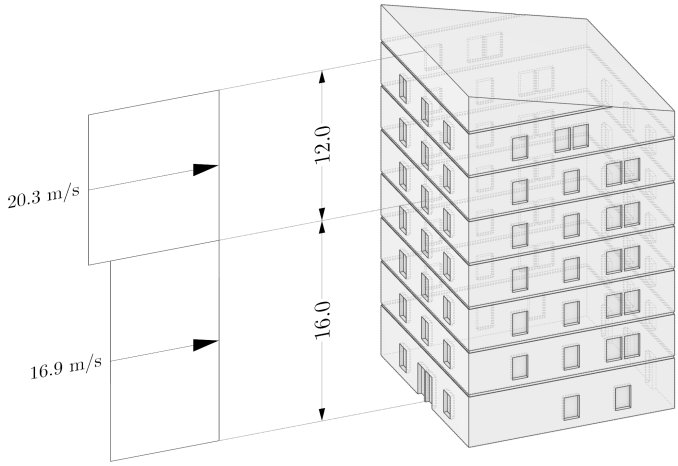

Figure 6.3: Wind speeds at height 16 meters and 28 meters

The dimensioning wind loads from *velocity pressure* is according to Eurocode calculated through Equation 6.3:

$$q_p = \Big[1 + 7 \cdot I_v\Big] \cdot q_b \tag{6.3}$$

where:

$$q_b = \frac{1}{2} \cdot \rho \cdot v_m^2 \tag{6.4}$$

$$I_v = \frac{k_I}{c_o \cdot \ln\left(\frac{z}{z_0}\right)} \tag{6.5}$$

Both Equation 6.4 and 6.5 vary according to height. The velocity pressures are also multiplied with the pressure coefficients for each location of the building corresponding to different pressure conditions at the walls and roofs. Specifically, for buildings of $e \leq d$, the distribution of pressure coefficient is in accordance to Figure 6.4, which together with Table 6.1, summarize the calculated pressure distributions on the building according to Eurocode. It is important to note the difference between q_b and q_p; the former represent the direct velocity pressure from the average wind speeds, while the latter represents the statistical maximum velocity pressure by considering the gust-factor and turbulence. The averaged value obtained from simulation is better compared with q_b, while q_p is used for design.

Table 6.1: Pressure coefficients, velocity pressures and design pressures for a singular building

	A1	A2	B1	B2	D1	D2	E1	E2	F	G	H
c_{p10} $[-]$	-1.2	-1.2	-0.8	-0.8	+0.8	+0.8	-0.54	-0.54	-2.5	-1.3	-0.9
v_m $[m/s]$	16.9	20.3	16.9	20.3	16.9	20.3	16.9	20.3	20.3	20.3	20.3
$q_b \cdot c_{p10}$ $[kN/m^2]$	-214	-309	-143	-206	143	206	-96	-139	-644	-335	-232
$q_p \cdot c_{p10}$ $[kN/m^2]$	-754	-958	-503	-639	503	639	-339	-431	-1997	-1038	-719

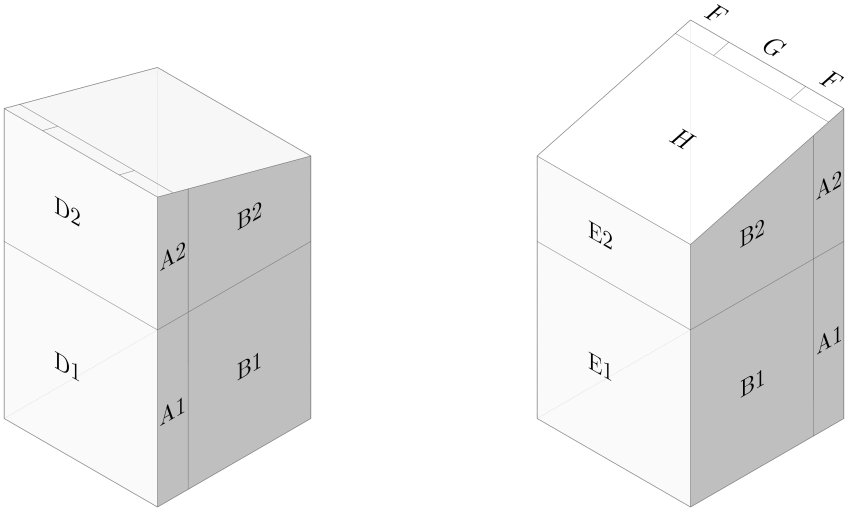

(a) Front of the building **(b)** Back of the building

Figure 6.4: Pressure coefficient zone distribution

6.2.2 Neighboring building

For the second part of the study, a neighboring building with identical footprint was placed 20 m directly in front, as shown in Figure 6.5. Whether this configuration sufficiently represents the blocking effect of a close urban environment, for either code application or simulation, is inconclusive due to the limited and varied definition of urban environment. Therefore, results serve primarily to support discussion rather than definitive conclusions.

The neighboring building has a height of 20 meters, representing the average surrounding building height h_{ave} in the immediate context.

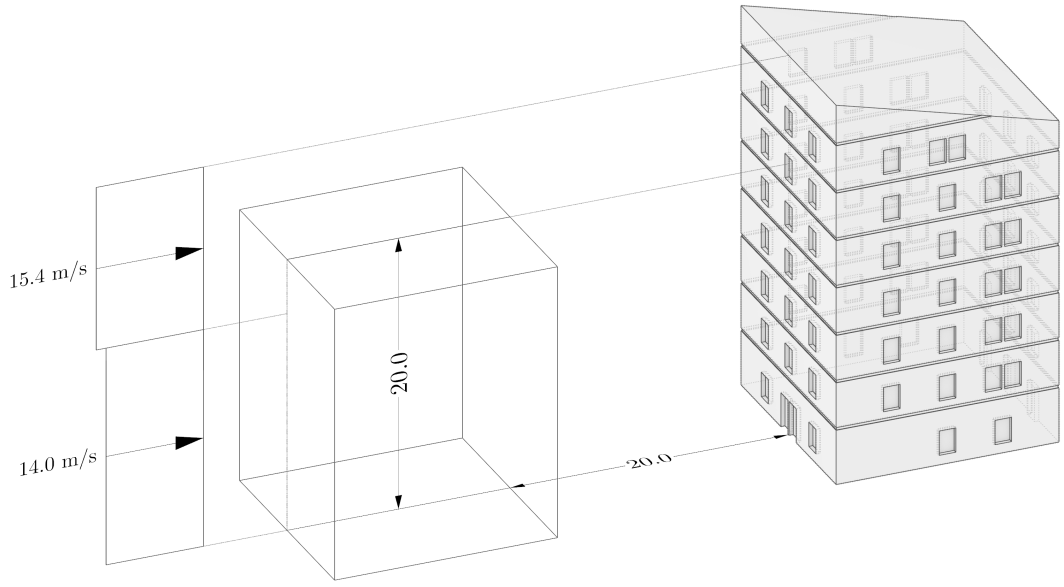

Figure 6.5: Neighboring building and wind velocities

The effect of the context essentially shielding the studied building can be taken into consideration using *Eurocode 1-1-4 Annex A.5: Displacement height*. If the distance to the neighboring buildings $x \leq 2 \cdot h_{ave}$, then h_{dis} is calculated by:

$$h_{dis} = \min \begin{pmatrix} 0.8 \cdot h_{ave} = 16\ m \\ 0.6 \cdot h = 16.8\ m \end{pmatrix} = 16\ m$$

The wind speed profile as well as the turbulence intensity profile is then raised by $h_{dis} = 16$ meters, which means effectively the bottom velocity is calculated at 0 meters and the top at 12 meters. Since the bottom velocity height is $0 < z_{min} = 10$ m, the height $z = 10\ m$ is instead considered for the bottom part, and $z = 28 - 16 = 12$ m for the top part. Going through the same steps as Equation 6.1 to 6.3, we achieve a final updated table of surface pressures:

Table 6.2: Pressure coefficients, velocity pressures and design pressures with a neighboring building

	A1	A2	B1	B2	D1	D2	E1	E2	F	G	H
c_{p10} $[-]$	-1.2	-1.2	-0.8	-0.8	+0.8	+0.8	-0.54	-0.54	-2.5	-1.3	-0.9
v_m $[m/s]$	14.0	15.1	14.0	15.1	14.0	15.1	14.0	15.1	15.1	15.1	15.1
$q_b \cdot c_{p10}$ $[kN/m^2]$	-148	-172	-98	-115	98	115	-66	-77	-358	-186	-129
$q_p \cdot c_{p10}$ $[kN/m^2]$	-596	-656	-398	-437	398	437	-268	-295	-1367	-711	-492

6.2.3 Simulation setup

To facilitate discussion about the relevance of numerical simulation to Eurocode-based design, both the stand-alone building and the configuration with a neighboring building were simulated. As stated, due to the inherent time-averaged nature of RANS-based simulation, it is more direct to compare the velocity pressure q_b, despite the fact these are not used for dimensioning. In principle, the velocity pressures achieved from CFD could be equated to q_b, and then converted into dimensioning velocity pressures q_p through the same steps as a fully empirical approach, similiar to the method presented in the AIJ guidlines, see Section 4.2.4 (Tominaga et al., 2008).

The inlet was defined with the velocity profile in accordance to Equation 6.2, however with a continuously variable height z:

$$u(z) = k_r \cdot \ln\left(\frac{z}{z_0}\right) \cdot u_{ref} \tag{6.6}$$

The kinematic turbulence intensity k is also defined at the inlet as:

$$k = \alpha(I \cdot u)^2 \tag{6.7}$$

where $\alpha = 1$, and I is calculated through Eurocode procedure as in Equation 6.5:

$$I(z) = \frac{k_I}{c_o(z) \cdot \ln(z/z_0)} \tag{6.8}$$

Since c_o and k_I are equal to 1 for this case, the turbulence intensity profile over height follows a simple inverse logarithmic distribution.

The turbulence intensity and velocity component of Equation 6.7 becomes:

$$I(z) \cdot u(z) = \left[\frac{1}{\ln(z/z_0)}\right] \cdot \left[k_r \cdot \ln\left(\frac{z}{z_0}\right) \cdot u_{ref}\right] = k_r \cdot u_{ref} \tag{6.9}$$

Simulation domain was set to 252 × 140 × 112 meters, with a base grid resolution of 18 × 10 × 8. Local refinement was increased to 6 levels for the building in contrast to the validation study, resulting in a smallest grid magnitude of roughly 0.2 meters. Maximum residual was set to 1×10^{-5}. For each simulation, the integrated Rhino-Grasshopper IBOFlow plugin was used, primarily to quickly switch simulation setup from singular building to building with neighbor.

6.2.4 Results

The simulation results primarily focuses on three metrics for both cases with and without a neighboring building:

Table 6.3: Comparison metrics for Case Study A.

	Measurement	Metric
1	IBOFlow simulation predicted pressures	q_{sim} $[kN/m^2]$
2	Difference between simulation pressures and the Eurocode pressures q_b	$q_{diff} = q_{sim} - (q_b \cdot cp_{10})$ $[kN/m^2]$
3	The difference expressed as a factor	$c_{diff} = \frac{q_{diff}}{q_b \cdot cp_{10}}$ $[-]$

A result indicating overall agreement between simulation and Eurocode would show c_{diff} values centered around zero without significant deviation. Positive values indicate overestimation by IBOFlow, while negative values indicate underestimation.

In Figure 6.6 (e), the c_{diff} values remain close to zero across most of the facade, indicating reasonable agreement between Eurocode and IBOFlow. Deviations appear primarily in localized areas near corners. Eurocode specifies larger pressure coefficients when performing detailed checks for areas approximately 1 meter in size, which aligns with both the observed higher velocity pressures in smaller regions captured by IBOFlow and the well-documented aerodynamic effects around corners of bluff bodies such as buildings.

The comparison with a neighboring building shows substantially larger deviations. If the simulation results are assumed to be predominantly accurate (which the first part without neighbor building suggests), Figure 6.6 (f) suggests that further investigation is warranted, either in the simulation setup or in the Eurocode method itself. The velocity pressure are as suggested by the results severely overestimated and underestimated at the bottom and top respectively. This raises questions about potential limitations in the Eurocode approach for accounting for neighboring building effects, which may explain why the Swedish National Annex prohibits the use of Annex A.5 (Displacement Height method).

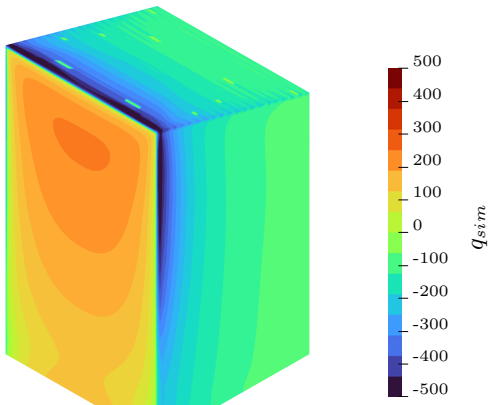

(a) q_{sim} without neighbor

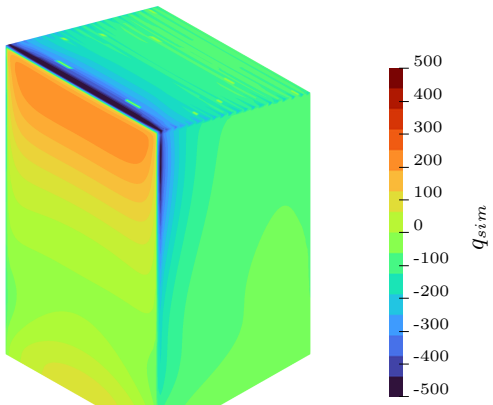

(b) q_{sim} with neighbor

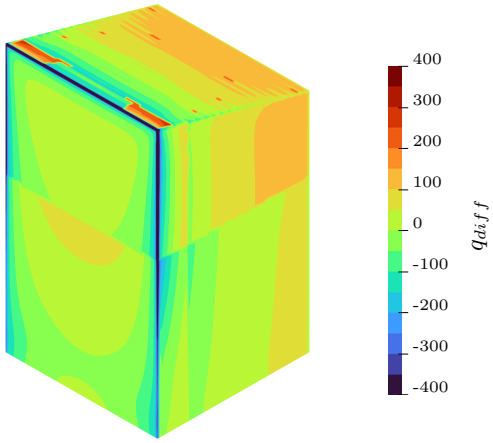

(c) q_{diff} without neighbor

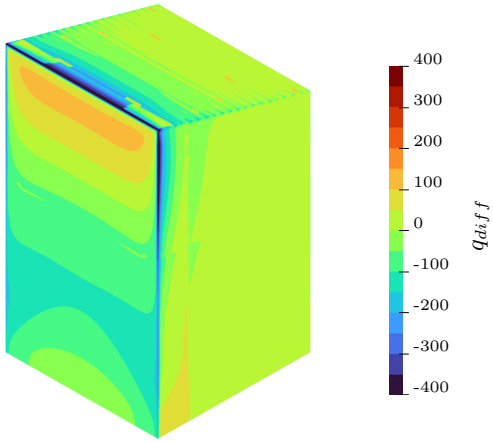

(d) q_{diff} with neighbor

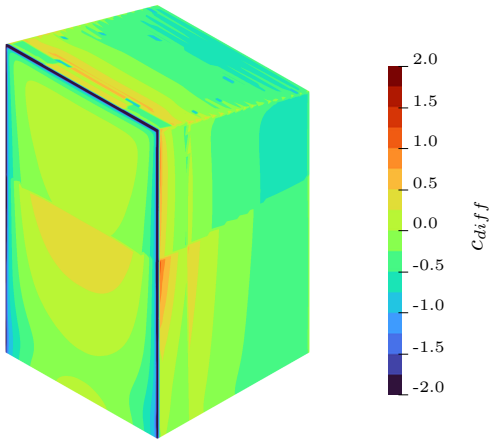

(e) c_{diff} without neighbor

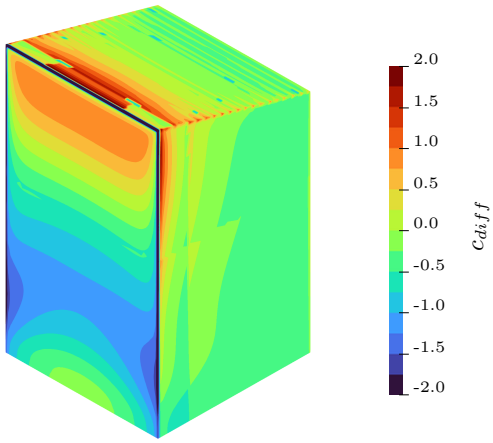

(f) c_{diff} with neighbor

Figure 6.6: IBOFlow results

6.3 Case B: High-rise shape study

High-rise buildings exceeding 200 m are excluded from Eurocode as the empirical equations are no longer valid, and wind tunnel studies are recommended instead. Conveniently, tall building projects typically have sufficient budget for wind tunnel testing. However, reliable wind tunnel studies are generally conducted only after key design parameters have been fixed. In-depth iterative aerodynamic optimization is not commonly performed during early architectural design stages or intermediate collaborative (architect-engineer) phases due to the time and cost associated with wind tunnel testing. This constraint limits the potential for achieving aerodynamically optimized designs in terms of structural performance.

Tamura et al. (2013) explored tall building aerodynamics by testing scale models of different typologies in a wind tunnel test and examining their respective aerodynamic and structural responses. This Case study explores how the proposed integrated IBOFlow method could enable similar aerodynamic and structural assessments during early-stage shape studies using a numerical approach. This is demonstrated by replicating portions of Tamura et al.'s study, condensing the wind response into a bending moment coefficient in the along-wind direction, and comparing with the wind tunnel data. Eight building typologies are tested.

All buildings are modeled at 1:1000 scale and share common characteristics. The height is consistently 400 mm, and the aspect ratio is approximately (H/B$\approx$ 8) across typologies, corresponding to a base width of approximately 50 mm with minor variations between configurations. The integrated IBOFlow plugin was utilized in order to change and launch simulation for each geometry faster.

The specific features and nomenclature for each typology are as follows:

a) **Square** is representative of an generic square building, in this context considered the "standard" case.
b) **Chamfer** has slightly larger base dimensions of 51 mm however also has a small modification of the base square where the corners are cut.
c) **Circular** is a slender cylinder shape, with a circle as the base.
d) **Tapered** has a larger square base measuring 69 mm width but tapers off to a 28 mm width at the top.
e) **Stepped** consist of four segments dividing the entire height, each segment having a square base of 69, 52, 28 and 41 mm.
f) **Opening** shares the dimensions of the base Square building, however the top features an opening to all four sides, measuring 16 mm wide and 83 mm tall.
g) **Helix** has the same square base but features an continuous twists of 180 degrees.
h) **Karl** has a slightly larger square base of 52 mm and also features a 90 degree twist of every corner roughly halfway up. This shape is not in Tamura et al.

Table 6.4: All studied building typologies

a) **Square**	b) **Chamfer**	c) **Circular**	d) **Tapered**
	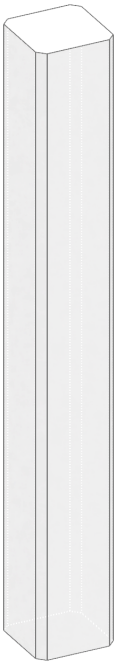		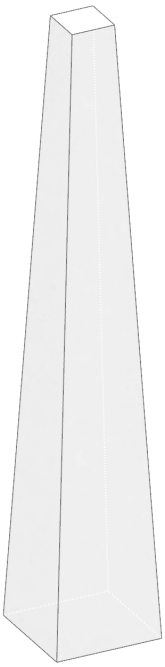
e) **Stepped**	f) **Opening**	g) **Helix**	h) **Karl**
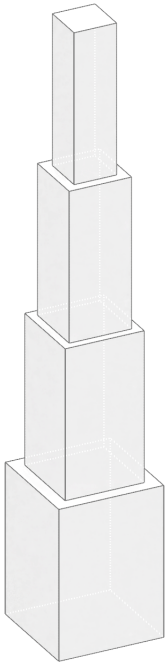			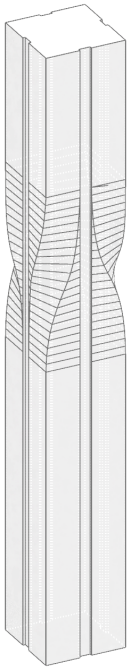

6.3.1 Simulation setup

The simulation was performed in an virtual replication of the wind tunnel experiment by Tamura et al (2013). In contrast to Case Study A, wind velocity at the inlet follows a power-law profile consistent with Japanese code:

$$u(z) = u_h \cdot \left(\frac{z}{z_h}\right)^{0.27} \tag{6.10}$$

where $u_h = 7.0\ m/s$ and $z_h = 0.4\ m$. Wind turbulence was measured across the height, and intensity at the top was $I_h = 9.2\%$. Japanese code use an inverse power-law profile for turbulence intensity, which in this case equates to:

$$I(z) = I_h \cdot \left(\frac{z}{z_h}\right)^{-0.27-0.05} \tag{6.11}$$

However, as the wind turbulence intensity over height was also recorded, a curve fit routine could be performed on the measured values, reflective of the k_{model} inlet in Section 4.2.2. These values do not follow the values predicted by the inverse power law. For this study, only the curve fit option was used for the simulation. The turbulence intensity I data is used in the definition of kinematic turbulent energy, assigned at the inlet, as:

$$k = (I \cdot U)^2 \tag{6.12}$$

Tamura et al. measured an overturning moment coefficient C_M for the entire building model by integrating the cross product between the resulting pressure forces F and the moment arm r, normalized by $q_h \cdot BH^2$:

$$C_M = \frac{\int M}{q_h \cdot BH^2} \tag{6.13}$$

where:

$$M = r \times F \tag{6.14}$$

$$q_h = \frac{1}{2}\ \rho \cdot u_h^2 \tag{6.15}$$

By condensing the results to a singular performance metric; the moment coefficient C_{MD}, for each typology, assessments can be made about both the aerodynamic performance of each design and the simulation accuracy compared to Tamura et al. (2013). However, the relative performance metric C_{MRel} (Equation 6.16), normalized against the Square baseline, provides a stronger validation argument.

$$C_{MRel} = \frac{C_{MD}}{C_{MD\_Square}} \tag{6.16}$$

In practical design scenarios, relative improvements between typologies are often more valuable than absolute values for informing shape optimization decisions. More importantly for validation purposes, if the relative performance trends predicted by IBOFlow align with those observed by Tamura et al., this demonstrates that the overall aerodynamic behavior is captured consistently. While this case study is not strictly intended as a formal validation, minimizing the influence of methodological differences strengthens the argument for IBOFlow's potential in early-stage aerodynamic optimization. The relative performance approach achieves this by focusing on comparative trends rather than absolute magnitudes.

6.3.2 Results

Table 6.5 shows the magnitudes of the moment coefficients C_{MD} for each typology. IBOFlow consistently underestimates the moment coefficient C_{MD} relative to Tamura et al., with the exception of the Helix typology. There is reasonable agreement between IBOFlow and Tamura et al., in particular for the Circular, Tapered and Stepped typology with results that are within 10% of the wind tunnel data.

Table 6.5: Moment coefficient for each typology

	Square	Chamfer	Circular	Tapered	Stepped	Opening	Helix	Karl
$C_{M\_IBOFlow}$	0.47	0.36	0.34	0.37	0.36	0.44	0.51	0.45
C_{M_Tamura}	0.60	0.50	0.38	0.43	0.40	0.55	0.53	-
Difference	0.13	0.14	0.04	0.06	0.04	0.11	0.02	-

Table 6.6 as well as Figure 6.7 show overall agreement in relative performance trends between IBOFlow and Tamura et al. The largest discrepancy occurs with the Helix typology, which IBOFlow overestimates. This deviation could stem from the steady-state nature of RANS simulation and the aerodynamic characteristics of the Helix geometry. The helical form has the largest projected area facing the wind yet performs favorably in the wind tunnel experiments of Tamura et al., presumably because its geometry mitigates predominantly dynamic effects such as vortex shedding and other turbulent flow interactions, which could contribute to the peak moments. IBOFlow cannot fully capture these dynamic characteristics and this limitation applies generally across typologies.

Table 6.6: Relative moment coefficient for each typology

	Square	Chamfer	Circular	Tapered	Stepped	Opening	Helix	Karl
$C_{MRel\_IBOFlow}$	1.00	0.78	0.73	0.80	0.76	0.95	1.09	0.97
C_{MRel_Tamura}	1.00	0.83	0.63	0.72	0.67	0.92	0.88	-
Difference	0.00	0.06	-0.15	-0.12	-0.15	0.03	0.21	-

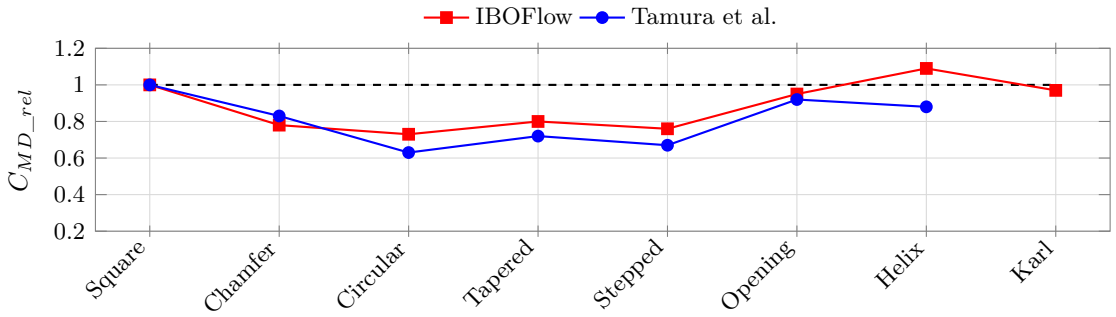

Figure 6.7: Trend of moment coefficient for each typology

Figure 6.8 to 6.11 illustrates another important consideration: local pressure coefficient distributions on specific facade regions may be of critical importance, particularly where sharp edges and corners of the bluff body experience larger velocity pressures. Full pressure coefficient results can be studied in Annex B.

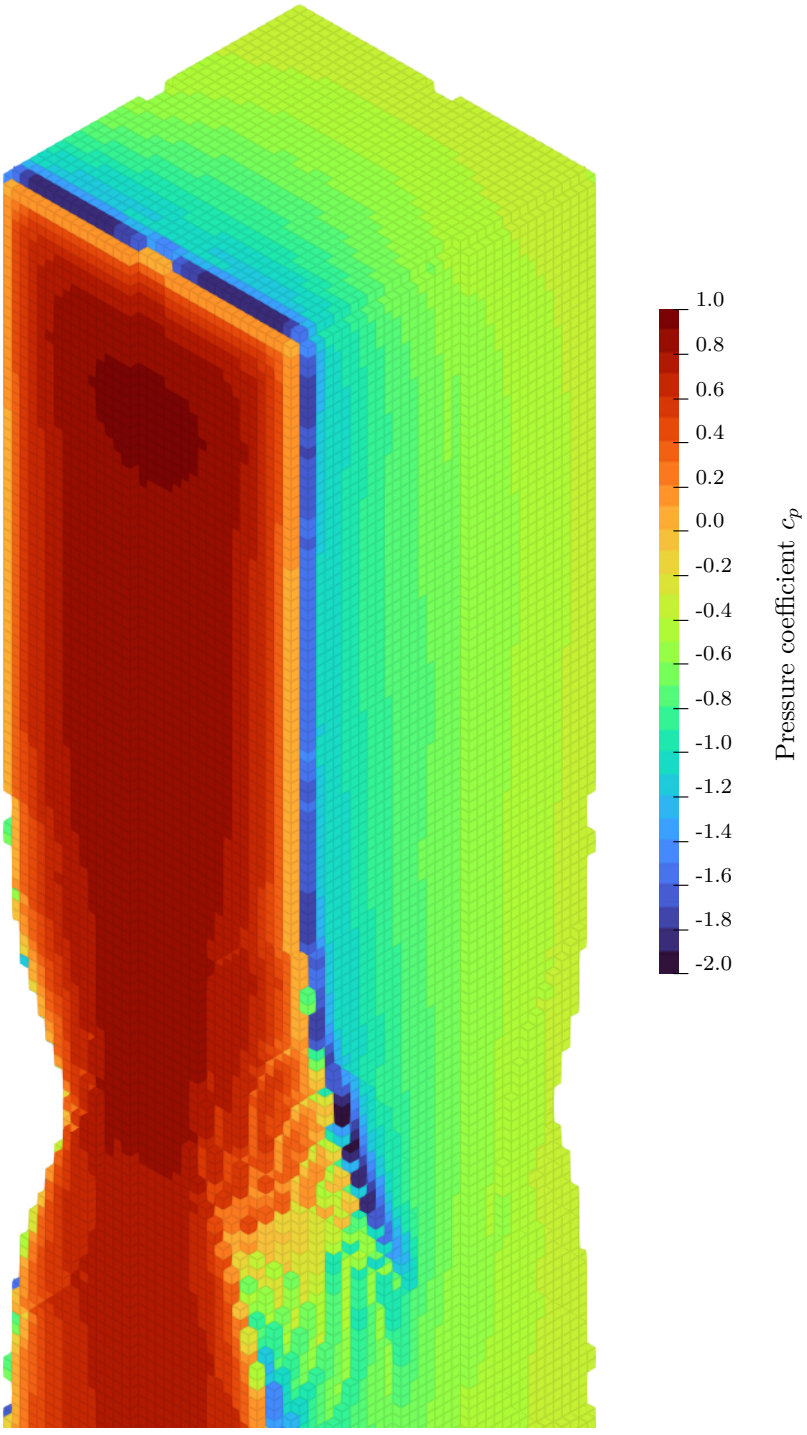

Figure 6.8: Pressure coefficient c_p distribution on Karl typology (part 1)

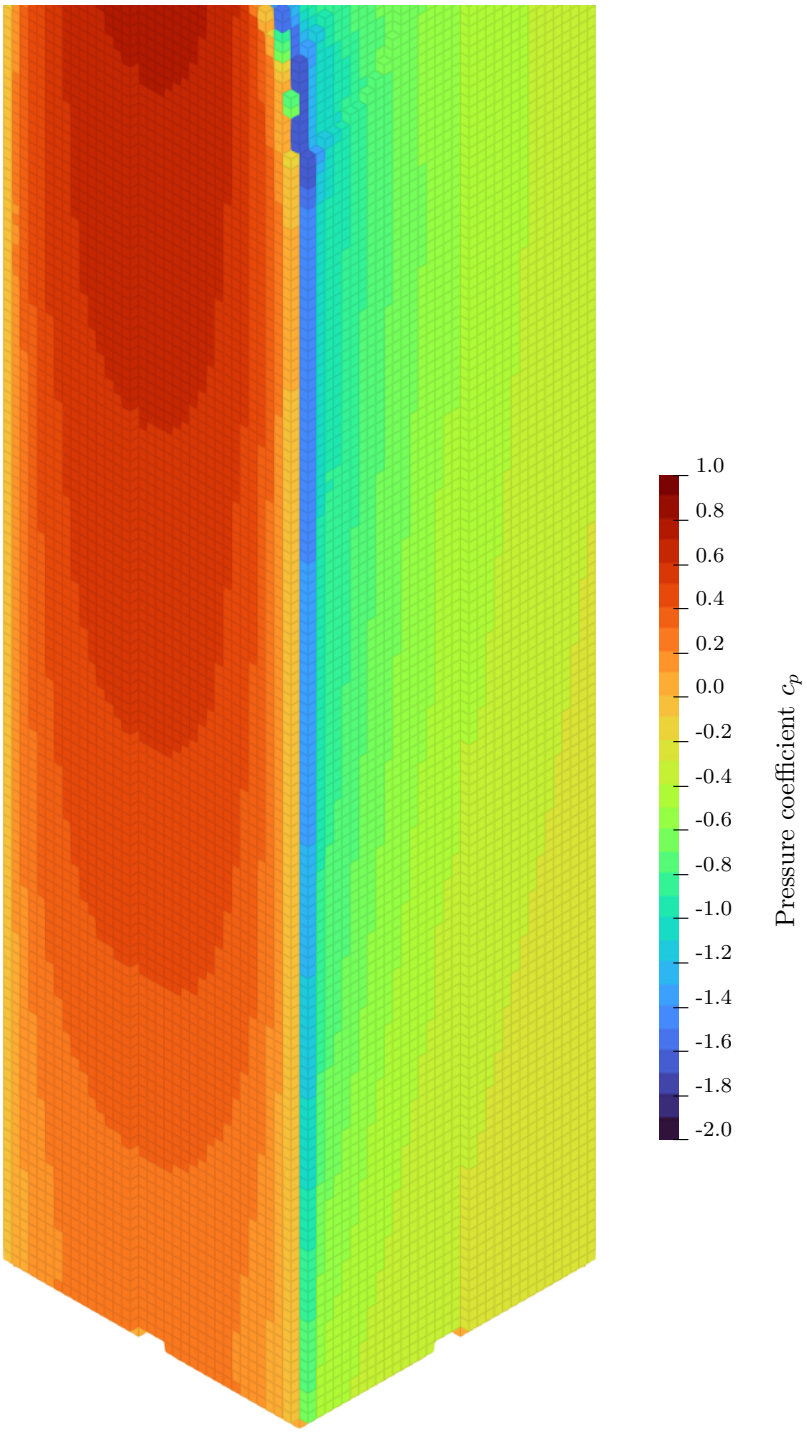

Figure 6.9: Pressure coefficient c_p distribution on Karl typology (part 2)

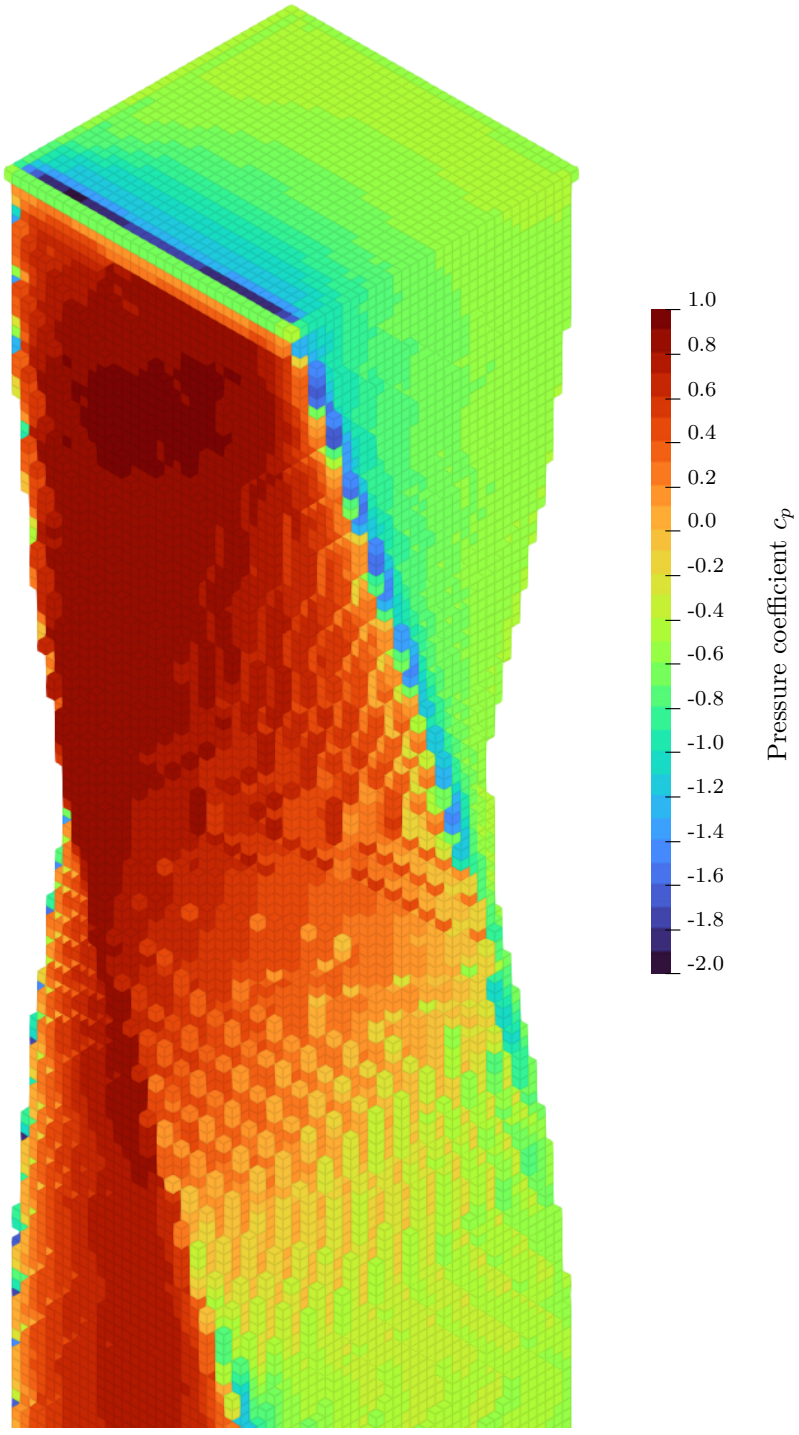

Figure 6.10: Pressure coefficient c_p distribution on Helix typology (part 1)

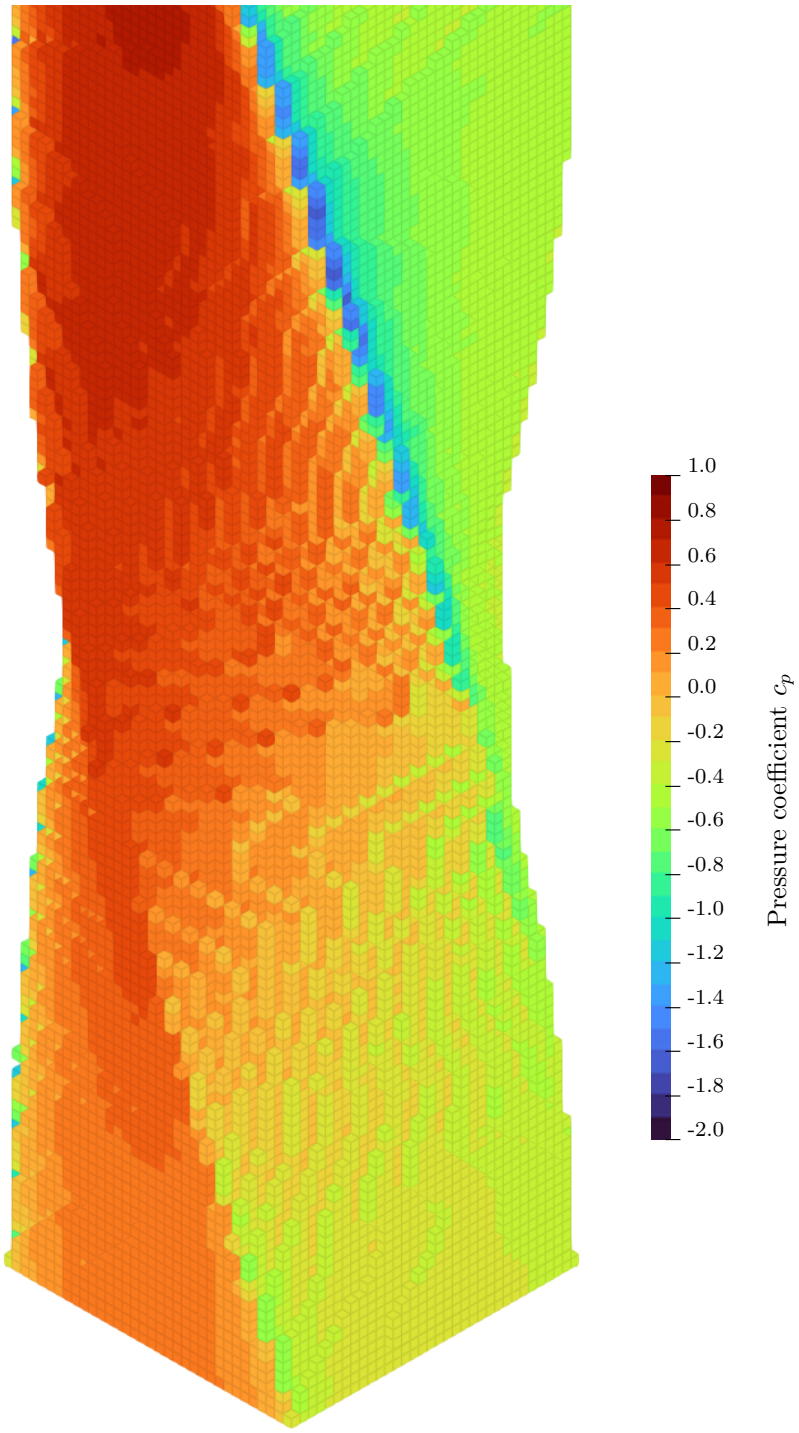

Figure 6.11: Pressure coefficient c_p distribution on Helix typology (part 2)

6.4 Case C: *Vertikal komposition*

The public artwork and sculpture *Vertikal komposition* was rebuilt in 2023. Its highly irregular shape presented a significant challenge to the structural engineers as it has practically no equivalence in code. Furthermore, both a wind tunnel study and/or a numerical simulation were deemed too expensive for the limited project budget. Instead, extrapolating from code together with qualified assumptions and findings from leading-edge research papers informed an empirically based estimate of the wind effects.

Two key concerns and one minor uncertainty was treated by the wind effects estimation done by the engineers: the pressure coefficient for the shape, the dynamic effects and lastly; the terrain category. Using IBOFlow and a RANS-based simulation, a static result is achieved and the dynamic effects cannot be treated properly. Therefore, this case study will investigate the potential of IBOFlow to assist in the minor uncertainty of terrain category, as well as the pressure coefficients for the complex shape presented, the results of the latter presented in Annex C.

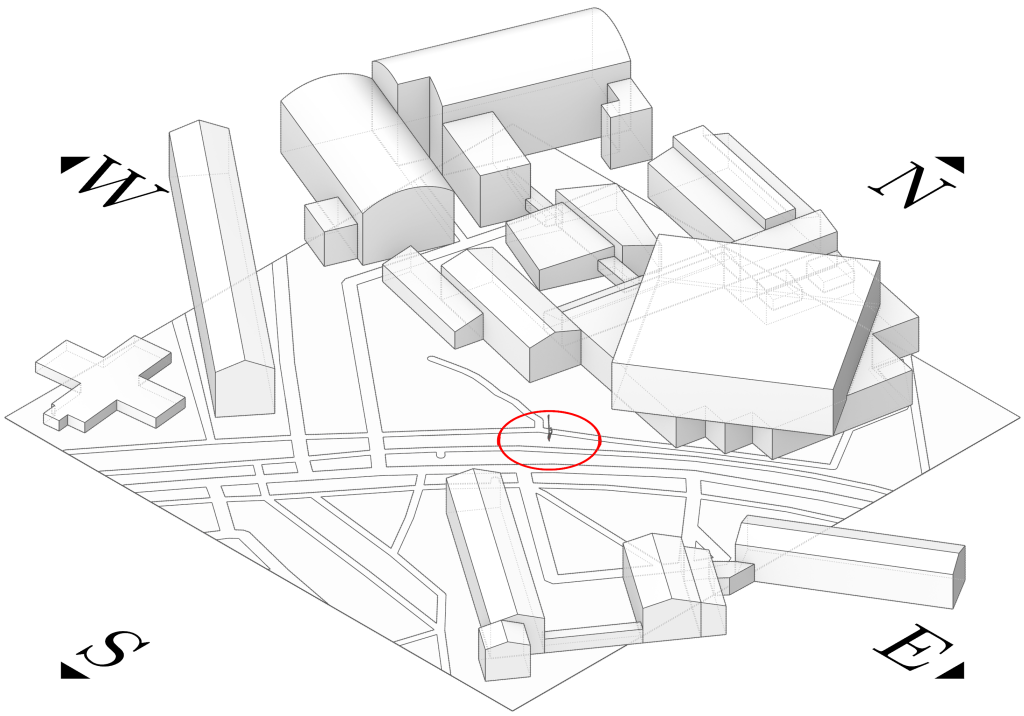

Figure 6.12: Situation and location of *Vertikal Komposition*

6.4.1 Simulation setup

Similar to Case Study A, the velocity and kinematic turbulent energy profile are defined using the Eurocode procedure for mean velocity and turbulent kinematic energy, $u(z)$ and $I_v(z)$ respectively. Two different constant inlet velocities are used: one defined at the reference height $z_{ref} = 7.5 \ \ m$ for the pressure coefficient study, and one defined as the base wind velocity $v_b = 26 \ \ m/s$.

For the terrain category investigation, the site was rotated at four different angles, to expose the sculpture to the inlet winds directly. The shape study investigated three different orientations against the wind denoted 0, 90 and 180 degrees respectively. Built-in Grasshopper functions were used to rotate the geometry, with the integrated IBOFlow plugins connected to the geometry handling of Grasshopper.

6.4.2 Results

The first part of the study investigates whether the assumed Terrain Category III is valid for the sculpture site. Qualitative analysis of the resulting wind speeds shows no obvious contradiction with this assumption: the sculpture location is shielded by surrounding buildings, resulting in reduced wind speeds at the site, as shown in Figure 6.13 a-b. Equation 6.17 present the resulting wind speed v_m from applying Equation 3.4 to the base wind speed $v_b = 26 \ \ m/s$, set at the inlet, evaluated at the height $z = 7.5 \ \ m$.

$$\begin{aligned} v_m &= v_b \cdot 0.19 \cdot \left(\frac{z_0}{z_{0,II}}\right)^{0.07} \cdot ln\left(\frac{z}{z_0}\right) \cdot c_o \\ &= 26 \cdot 0.19 \cdot \left(\frac{0.3}{0.05}\right)^{0.07} \cdot ln\left(\frac{7}{0.3}\right) \cdot 1 \\ &= 18.03 \ \ m/s \end{aligned} \tag{6.17}$$

The sculpture is more exposed to winds from the south, as shown in Figure 6.13 c-d, where the wind velocity approaches 18 m/s as predicted by Equation 6.17.

The second part investigates whether the sculpture shape can be assumed to behave aerodynamically as a triangular prism in terms of pressure coefficients. The results are presented in Annex C. Assuming the simulation results are accurate, the rounded corners of the sculpture geometry alter the flow behavior considerably, resulting in regions of higher pressure compared to a sharp-edged triangular geometry. This can be understood intuitively: the rounded corners allow the moving air to remain attached to the surface rather than separating. These results can be compared to the studies performed by Abdusemed et al. (2015), and Jendzelovsky et al., (2017).

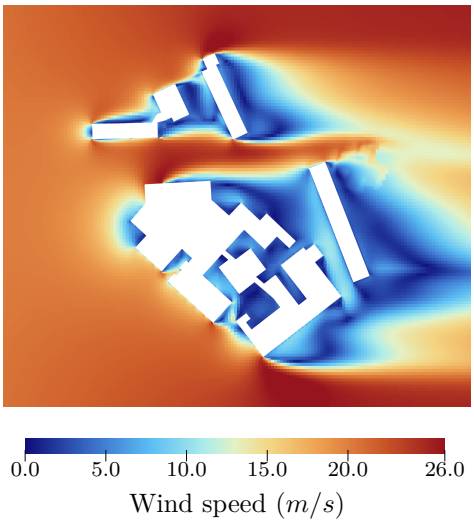

(a) Wind from north

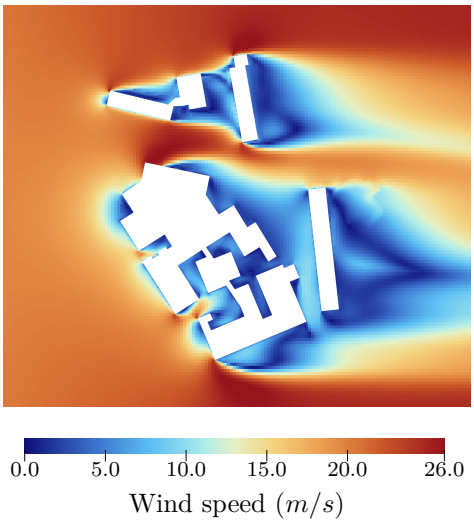

(b) Wind from north-west

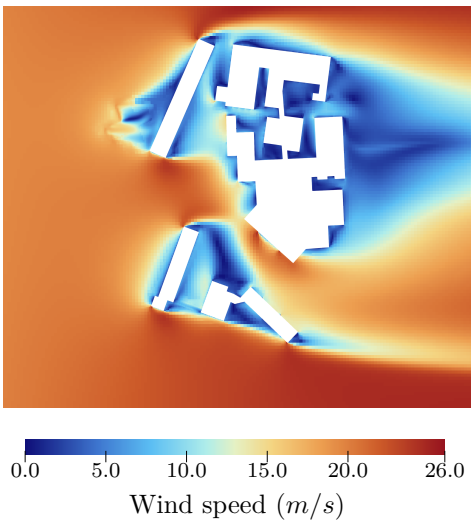

(c) Wind from south

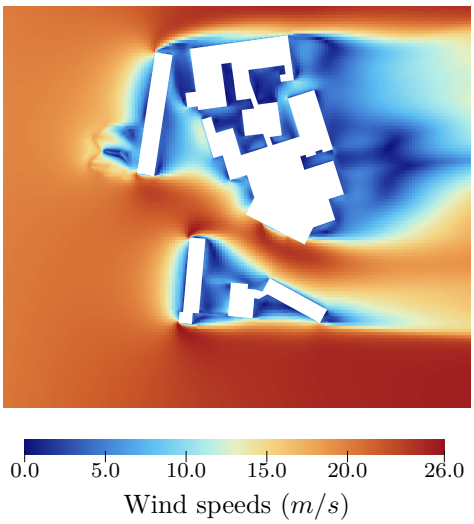

(d) Wind from south-west

Figure 6.13: Comparison of wind speeds depending on direction relative to inlet

7
Discussion

In summary, the thesis Aims outlined in Section 1.2 have been addressed through the following chapters:

- *Provide an overview of fundamental fluid mechanics, and its relation to empirical design codes, particularly Eurocode.*
  - ✔ Chapter 2: Fluid mechanics fundamentals; and Chapter 3: Wind loads on buildings.
- *Outline the current challenges going from empirical data to numerical methods.*
  - ✔ Chapter 4: Computational Wind Engineering.
- *Test and validate simulation methods in a structural design context.*
  - ✔ Chapter 5: Validation of IBOFlow
- *Implement, and test new CFD methods and evaluate the potential as well as relevance.*
  - ✔ Chapter 6: Case Studies.

These chapters will now serve as the basis for the final summary, discussion and outlook.

7.1 CWE, Structural Design and IBOFlow

Alan Garnett Davenport's early emphasis on wind tunnel analysis underscores the long-standing importance of aerodynamic considerations in structural design. The emergence of Computational Wind Engineering has since further demonstrated the growing potential of numerical wind simulation. Computational Fluid Dynamics is gaining broader recognition with the inclusion in the second-generation of Eurocode. However, formal inclusion in a standard does not, by itself, increase the practical usefulness of CFD. The potential of CFD is still reliant on further validation efforts, establishment of specific best-practice guidelines, and – central to this thesis – the development of accessible CFD frameworks for structural engineers, particularly in terms of setup complexity and hardware requirements.

The following review summarizes the current landscape of CWE as it relates to this thesis.

7.1.1 Comparison of computational efficiency

Xing et al. (2022) used a Large Eddy Simulation (LES) approach to evaluate wind loads on Torre Gioa 22, a high-rise building in Milan, Italy. The tower's irregular and angular geometry, as well as the complex urban surrounding made it a clear example of structures that fall outside standard code classifications. The authors note that for a large-budget projects, the relative time and cost drawbacks of a wind tunnel test are often less impactful than the

uncertainty and limited credibility of CFD in practice.

Similair to Case Study A and C of this thesis, the boundary conditions were defined according to Eurocode wind and turbulence profiles. A key difference, however, was their use of transient LES simulation in contrast to the steady-state RANS simulation in IBOFlow.

The LES simulation achieved results comparable to a wind tunnel test in terms of pressure coefficient (c_p), although a consistent underestimation of suction was (also) observed. Each simulation was run on a large HPC cluster comprising 1022 nodes (processor units), requiring approximately 5000 core hours (around 10 minutes of real time per run). The estimated computational cost, ranging between €3,000 and €50,000, limits the argument for CFD as a universally cost-effective alternative.

By contrast, the methodology developed in this thesis – using IBOFlow on consumer-grade laptop hardware – achieved comparable agreement with validation-case wind tunnel data at negligible running costs. The runtime for the validation case presented in Section 5.2.4 was 2.2, 12.9, and 90.1 minutes for grid levels G1, G2, and G4 respectively, corresponding to approximately 0.3, 1.7, and 12 core-hours on an 8-core system. This illustrates the potential of accessible methods, such as the Immersed Boundary approach, to deliver quick results on standard hardware.

7.1.2 Static and dynamic simulation

Another study by Xing et al (2023) used CFD as an early-stage design tool for the New Bologna Stadium roof. Similar to the aim of this thesis, their work positioned CFD results as a means of estimating wind effects to guide design during early phases. The large roof spans and the site's location, featuring a nearby hill, introduced aerodynamic complexity that Eurocode cannot easily capture.

The authors concluded that structural damping and the dynamic effects – obtainable from transient LES – were more significant than static forces, for a lightweight structure like a stadium roof. This emphasizes the need for caution when interpreting steady-state RANS results, such as those generated by IBOFlow, for structures where dynamic wind responses are expected to dominate.

7.1.3 Complex geometry analysis

Zhang et al. (2020) investigated a direct optimization routine connected to CFD results. This automated approach remains as an natural progression of this thesis, with the developed interface between 3D CAD software (Rhino 3D) and IBOFlow. Their paper, while lacking extensive validation, achieved an 67% reduction of aerodynamic forces *in vitro*, by using the automated optimization algorithm, demonstrating the large potential of in-depth integration of CFD.

Furthermore, Jendzelovsky et al. (2017) investigated irregular, triangular, high-rise structures with curved corners using CFD. Since Eurocode primarily provides guidance for square and regular building plans, estimating wind loads for smooth triangular shapes is not straightforward. The authors noted a different drawback of wind tunnels (except for time and cost):

without prior empirical data, it is challenging to know the optimal placement of physical pressure sampling points in order to capture peak values.

In contrast, CFD provides a calculated value at every modeled part of the structure. This is illustrated in Case Study B, where the Helix and Karl typologies exhibited large peak pressure coefficients on very specific parts of the facade. Such conditions may present larger challenges for cladding and local structural design compared to the building's overall aerodynamic performance and base overturning moment.

In their work, Jendzelovsky et al, found an overall difference between CFD and wind tunnel test of approximately 6%, with CFD again tending to underestimate negative pressures on the leeward side. Their closing conclusion is that a hybrid approach, utilizing CFD in conjunction with wind tunnel testing, is a powerful combination for providing useful estimates at different design stages.

7.1.4 Future directions in code

The field of Computational Wind Engineering is demonstrably active and expected to expand further with the inclusion of CFD in the next-generation Eurocode. In a "Review for the practical application of CFD for determination of wind load on high-rise buildings", Thordal et al. (2019) note that CFD has already become a promising and, to some extent, established tool in building design, particularly as computational efficiency improves and results become more accessible. However, the authors emphasize that the absence of established best-practice guidelines continues to limit CWE applications primarily to early design phases. Similar to Jendzelovský et al., they also note the power of a hybrid approach of CFD and wind tunnel experiments.

The idea of placing CFD tools directly in the hands of structural engineers often raises concerns among CFD experts, who are well-informed of the inherent challenges in producing reliable CFD results. Nevertheless, with increased recognition, the interest in CFD is likely to continue to grow and the critical question then becomes how best to meet this rising demand safely and effectively, rather than unequivocally rejecting the effort.

In terms of standardization, the Architectural Institute of Japan (AIJ) is notably ahead, having already produced guidelines for both transient LES and steady-state RANS simulations. For instance, the AIJ recommends sampling LES simulations over periods that capture the probabilistic nature of real-world peak wind velocities, while RANS results are treated as representative of mean values – appropriate for evaluating global structural responses such as overturning moments.

An updated Eurocode could benefit from following a similar model, expanding its scope to include recommendations on CFD setup, domain sizing (to minimize blockage effects), and appropriate inlet conditions for wind velocity and turbulence profiles.

Equally important is the codification of interpreting result. For example, the consistent tendency of RANS to underestimate negative pressures on the leeward side could be addressed through the introduction of CFD-specific safety factors or confidence intervals.

Finally, as highlighted by Vanky et al. (2024), current existing (but limited) guidelines does

not address the Immersed-Boundary method yet. Although the method shows promising performance, especially its scalability on accessible hardware, its general acceptance and widespread adoption depend on the establishment of similarly rigid guidelines that produce repeatable and consistent results.

7.2 Further research

The work presented in this thesis establishes the viability and accessibility of the integrated IBOFlow method for early-stage structural wind analysis. Validation results confirmed that IBOFlow can deliver usable predictions of pressure distributions on regular buildings while maintaining good computational performance on consumer hardware. Case Studies A, B, and C illustrated scenarios in which IBOFlow could help intepratation of code usage and assist in early stage design.

The following areas represent natural extensions of this research:

Dynamic Simulation
The current RANS-based IBOFlow simulation is limited to steady-state, time averaged pressures. As an next step, URANS (Unsteady RANS) could be used to investigate and capture dynamic effects such as vortex shedding or aeroelastic interactions through Fluid-Structure Interaction (FSI). Results from Case Study B, where the Helix typology likely benefits from dynamic aerodynamic behavior, showed noticeable discrepancies that could be better resolved using transient approaches.

Uncertainty and Safety Factors
To bring IBOFlow closer to practical design applications, the inherent uncertainties in simulation outputs should be better quantified. Averaged RANS results could be treated as representative of mean wind conditions, that is then treated with an probabilistic gust factor as well as safety factors. The first part of Case Study A demonstrated overall close results between IBOFlow and Eurocode in the standard case when comparing the "raw" velocity pressures, not yet treated with gust factors and turbulence. The safety factors could be CFD specific, to address for example the consistent underestimation of leeward facade suction.

Expanded integration and user-interface
The interface between Rhino 3D and IBOFlow could be further refined to improve both usability and interoperability. Enhancing interface between the simulation and design environments – such as visualizing pressure fields directly within Rhino 3D, exporting pressure maps for use in finite element analysis, or integrating automated optimization workflows – would significantly strengthen IBOFlow's value as a practical design tool. Such developments would also align closely with the automation efforts demonstrated by Zhang et al. (2020).

7.3 Conclusion

Based on the work presented in this master's thesis, the following concluding remarks can be made:

- Computer Wind Engineering is still gradually growing, but has a few roadblocks in order to gain further recognition.
- European design codes does not yet universally incorporate integration of CFD based methods in an standardized way.
- Existing CWE guidelines rarely address the Immersed Boundary (IB) method, and are usually tailored for estimating pedestrian wind comfort.
- The IB method presents an attractive balance between computational speed and user accessibility.
- IBOFlow has before this thesis not yet been applied to a structural design setting. The Immersed Boundary method sees relatively limited application overall, no less true for buildings and structural applications.
- Validation results show that IBOFlow can deliver reliable, usable predictions for early-stage analysis.
- However, uncertainties in CFD, including those specific to RANS modeling, currently position IBOFlow primarily as a predictive tool rather than a definitive design method.
- The case studies presented demonstrate the practical usability of an integrated IBOFlow workflow and identify contexts in which CFD tools hold particular relevance: code interpretation and early design guidance.

Bibliography

[1] Boverket (1997) *Boverkets handbok om snö- och vindlast* (Second edition). Boverket: Byggavdelningen. Retrieved from: [Link]

[2] Simiu E., Yeo D. (2019) *Wind Effects on Structures: Modern Structural Design for Wind* (Fourth Edition). John Wiley & Sons Ltd. ISBN 9781119375937

[3] Solari, G. (2019) *Wind Science and Engineering: Origins, Developments, Fundamentals and Advancements*. Springer Tracts in Civil Engineering. ISBN 9783030188146

[4] Bilah K., Scanlan R. (1990) *Resonance, Tacoma Narrows bridge failure, and undergraduate physics textbooks*. The John Hopkins University: Department of Structural Engineering. Retrieved from: [Link]

[5] SIS/TK 203 Eurokoder (2005) *Eurocode 1: Actions on structures - Part 1-4: General actions - Wind actions* (SS-EN 1991-1-4:2005). SIS. Retrieved from: [Link]

[6] Elmisaoui S., Kissami I., Ghidaglia, J.M. (2024) *High-Performance Computing to Accelerate Large-Scale Computational Fluid Dynamics Simulations: A Comprehensive Study*. Springer Retrieved from: [Link]

[7] Statens Konstråd (2023) *Vertikal Komposition - Så återskapades ett kulturarv*. Retrieved from: [Link]

[8] Gibiansky A. (2011) *Fluid Dynamics: The Navier-Stokes Equations*. Retrieved from: [Link]

[9] Waterman S. (2024) *Lecture Notes for EOSC 512: Advanced Geophysical Fluid Dynamics (GFD)*. The University of British Columbia: Department of Earth, Ocean and Atmospheric Sciences. Retrieved from: [Link]

[10] SimScale GmbH (2024) *SimScale Documentation*. Retrieved from: [Link]

[11] Fagerström M., Brouzoulis J. (2021) *Lecture Notes for VSM167: Finite Element Method Basics*. Chalmers University of Technology: Department of Industrial and Material Science

[12] Barber J.R. (2010) *Elasticity*. (Third Edition). Springer Tracts in Civil Engineering. ISBN 9789048138081

[13] Clay Mathematics Institute (2025) *Navier-Stokes Equation*. Retrieved from: [Link]

[14] George W.K. (2013) *Lectures in Turbulence for the 21st Century*. Chalmers University of Technology: Department of Applied Mechanics

[15] Andersson N. (2024) *Lecture Notes for MTF053: Fluid Mechanics*. Chalmers University of Technology: Department of Mechanics and Maritime Sciences. Retrieved from: [Link]

[16] Davidson L. (2024) *An Introduction to Turbulence Models*. Chalmers University of Technology: Department of Mechanics and Maritime Sciences. Retrieved from: [Link]

[17] An, L.S., Alinejad, N., Kim S., Jung S. (2023) *Experimental study on wind characteristics and prediction of mean wind profile over complex heterogeneous terrain*. University of Michigan: Department of Civil and Environmental Engineering. Retrieved from: [Link]

[18] Picozzi V., Sepe V., Avossa A.M., Ricciardelli F. (2025) *Probabilistic framework for the calibration of mean wind profiles in urban areas*. University of Campania: Department of Engineering. Retrieved from: [Link]

[19] Holmes J.D. (2015) *Wind Loading of Structures* (Third Edition). CRC Press: Taylor & Francis Group. ISBN 9781482229226

[20] Bashor R., Kareem A., Moran R. (2009) *Comparative study of major international standards*. University of Notre Dame: NatHaz Laboratory. Presented at: The Seventh Asia-Pacific Conference on Wind Engineering. Retrieved from: [Link]

[21] Sadeghi Y.M. (2021) *Introduction to Fluid-Structure Interactions* (First Edition). Springer Nature Switzerland. ISBN 9783030858841

[22] Blocken, B. (2014) *50 years of Computational Wind Engineering: Past, present and future*. Eindhoven University of Technology: Department of the Built Environment. Retrieved from: [Link]

[23] Cochran L., Derickson R. (2011) *A physical modeler's view of Computational Wind Engineering*. Published in: Journal of Wind Engineering and Industrial Aerodynamics 99. Retrieved from: [Link]

[24] Stathopoulos T. (1997) *Computational wind engineering: Past achievements and future challenges*. Concordia University: Centre for Building Studies. Published in: Journal of Wind Engineering and Industrial Aerodynamics 67. Retrieved from: [Link]

[25] Thordal M., Bennetsen J., Koss H. (2019) *Review for practical application of CFD for the determination of wind load on high-rise buildings*. Technical University of Denmark. Published in: Journal of Wind Engineering and Industrial Aerodynamics 186. Retrieved from: [Link]

[26] Hansen S.O., Höffer R., Rees J., Ricciardelli F., Spehl P. (2019) *Towards the Second Generation Eurocodes: Evolution of EN 1991-1-4 Wind Actions*. Springer Nature Switzerland AG 2019. Published in: Proceedings of the XV Conference of the Italian Association for Wind Engineering. Retrieved from: [Link]

[27] Ricciardelli F. (2023) *prEN 1991-1-4:2021: the draft Second Generation Eurocode on wind actions on structures - A personal view*. University of Campania "Luigi Vanvitelli": Department of Engineering. Retrieved from: [Link]

[28] Tamura T., Nozawa K., Kondo K., (2008) *AIJ guide for numerical prediction of wind loads on buildings*. Tokyo Institute of Technology. Published in: Journal of Wind Engineering and Industrial Aerodynamics 96. Retrieved from: [Link]

[29] CFD Online, (2016) *SIMPLE algorithm*. Retrieved from: [Link]

[30] Franke J., Hellsten A., Schlünzen H., Carissimo B., (2007) *Best practice guideline for the CFD simulation of flows in the urban environment*. University of Hamburg: Centre for Marine and Atmospheric Sciences. ISBN 3000183124

[31] Tominaga Y, Mochida A, Yoshie R, Kataoka H, Nozu T, Yoshikawa M, Shirasawac T. (2008) *AIJ guidelines for practical applications of CFD to pedestrian wind environment around buildings*. Niigata Institute of Technology. Published in Journal of Wind Engineering and Industrial Aerodynamics 96. Retrieved from: [Link]

[32] Mitkov R., Hristov P.O., Hunger F., Mark A. (2024) *On the variety and adequacy of different solution verification approaches in computational wind engineering*. GATE Institute. Retrieved from: [Link]

[33] IBOFlow (2025) *IPS IBOFlow*. Retrieved from: [Link]

[34] Mark A., Rundqvist1 R., Edelvik F. (2011) *Comparison between different immersed boundary conditions for simulation of complex fluid flows*. Fraunhofer-Chalmers Center (FCC). Retrieved from: [Link]

Evaluation of an immersed boundary numerical framework to address the wind field in complex urban topographies

[35] Vanky P., Mark A., Hunger F., Sardina G., et al. (2024) *Evaluation of an immersed boundary numerical framework to address the wind field in complex urban topographies.* Chalmers University of Technology: Department of Mechanics and Maritime Sciences. Retrieved from: [Link]

[36] Vanky P. (2023) *Numerical Simulations of the Urban Microclimate.* Chalmers University of Technology: Department of Mechanics and Maritime Sciences. Retrieved from: [Link]

[37] Montazeri H, Blocken B. (2012) *CFD simulation of wind-induced pressure coefficients on buildings with and without balconies: Validation and sensitivity analysis.* Eindhoven University of Technology: Building Physics and Services. Published in Building and Environment Volume 60. Retrieved from: [Link]

[38] Boverket (2022) *Boverkets föreskrifter och allmänna råd om tillämpning av europeiska konstruktionsstandarder (eurokoder).* Boverket: Byggavdelningen. Retrieved from: [Link]

[39] Tamura Y., Kim Y.C., Tanaka H., Bandi E.K., Yoshida A., Ohtak K. (2013) *Aerodynamic and Response Characteristics of Supertall Buildings With Various Configurations.* Tokyo Polytechnic University. Published in The Eighth Asia-Pacific Conference on Wind Engineering. Retrieved from: [Link]

[40] Vrouwenvelder T., Scholten N. (2010) *Assessment Criteria for Existing Structures.* Delft University of Technology: Faculty of Civil Engineering and Geosciences. Retrieved from: [Link]

[41] Baravelle M., Köhler J. (2018) *On the probabilistic representation of the wind climate for calibration of structural design standards.* Norwegian University of Science and Technology: Department of Structural Engineering. Published in: Structural Safety Volume 70. Retrieved from: [Link]

[42] Abdusemed A.M., Ahuja K. A. (2015) *Wind Pressure Distribution on Triangular Shape Tall Buildings.* Published in: International Journal of Innovative Research in Science, Engineering and Technology Volume 4. Retrieved from: [Link]

[43] Jendzelovsky N., Antal R., Konecna L. (2017) *Investigation of the External Pressure Coefficients on the Facade of the Triangular High-Rise Structure with Curved Corners.* Slovak University of Technology in Bratislava: Faculty of Civil Engineering. Published in: Procedia Engineering Volume 190. Retrieved from: [Link]

[44] Xing K., Patruna L., Pozzuolu C., Pedro G., Miranda S., Ubertini F. (2022) *Wind loads prediction using LES: Inflow generation, accuracy and cost assessment for the case of Torre Gioia 22.* University of Bologna. Published in: Engineering Structures 262. Retrieved from: [Link]

[45] Xing J., Patruna L., Miranda S., Pinardi S., Majowiecki M., Ubertini F. (2023) *Early stages wind load assessment using Computational Fluid Dynamics: The new Bologna Stadium roof.* University of Bologna. Published in: Structures 47. Retrieved from: [Link]

[46] Zhang R., Waibel C., Wortmann T. (2020) *Aerodynamic Shape Optimization for High-Rise Conceptual Design: Integrating and Validating Parametric Design, (Fast) Fluid Dynamics, Structural Analysis and Optimization.* ETH Zürich. Conference paper at: eCAADe 2020 Retrieved from: [Link]

A

Grasshopper plugin components

Table A.1: Table of all custom Grasshopper components and their respective function.

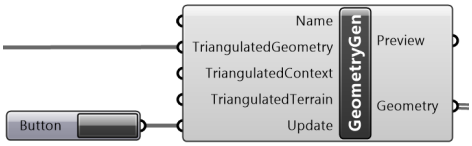	The "Geometry" component automatically converts the triangulated mesh into an .stl file and saves it in a local folder. The main importance of .stl is its compatibility with .vtk, a similar format which in turn is compatible with IBOFlow.
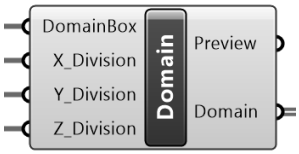	In the second component, "Domain", the simulation domain and location of the physical boundaries are set.
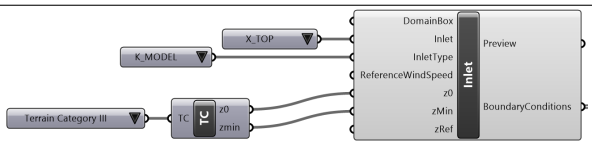	The third component, "Inlet" assigns the inlet boundary conditions.
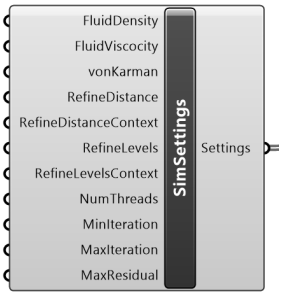	The fourth component is the last one of the setup; "SimSettings". General information about the fluid and the simulation are set here.
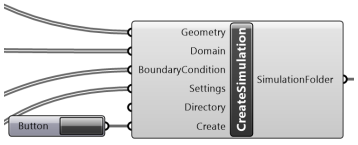	Component one to four are all collected by the fifth component, "CreateSimulation", which exports the geometry and settings into a simulation folder.
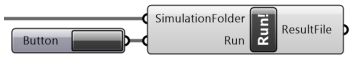	The final component "Run!" takes the simulation folder and launches the simulation directly from Grasshopper using a subprocess-routine.

B

Case study B: Expanded results

This Annex presents the full results of pressure coefficients distribution plots for each Typology in Section 6.3.

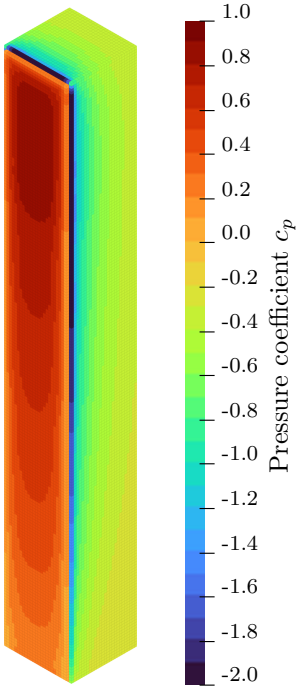

(a) Standard

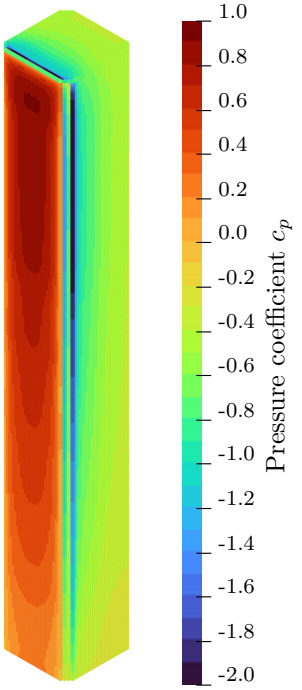

(b) Chamfer

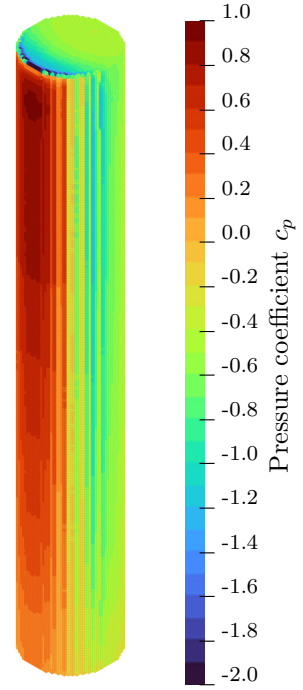

(a) Circular

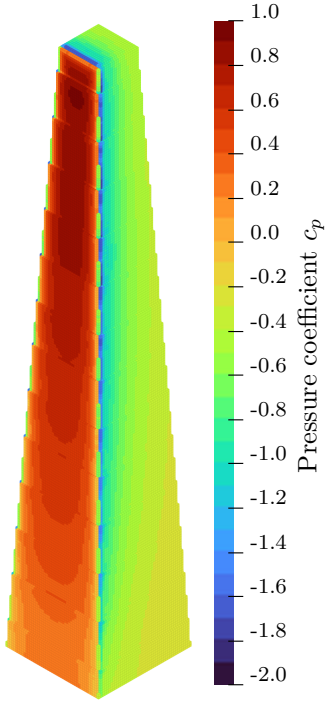

(b) Tapered

Figure B.1: Distribution of pressure coefficients c_p for each typology.

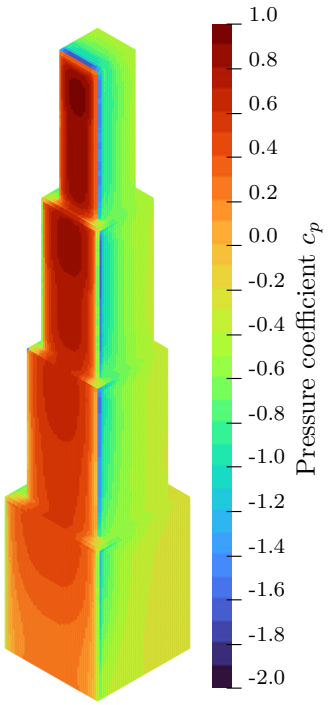

(a) Stepped

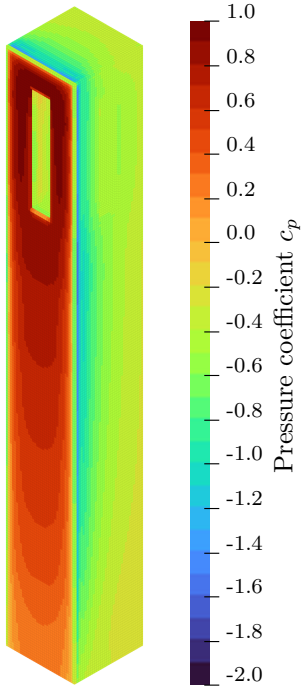

(b) Opening

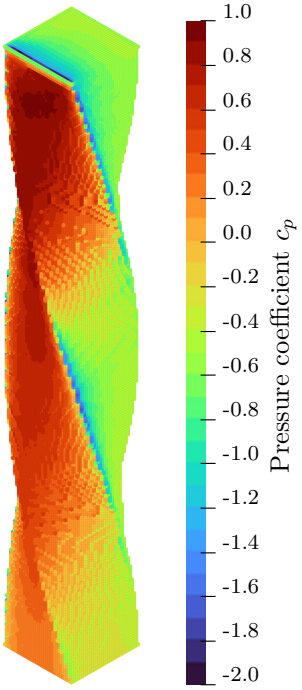

(a) Helix

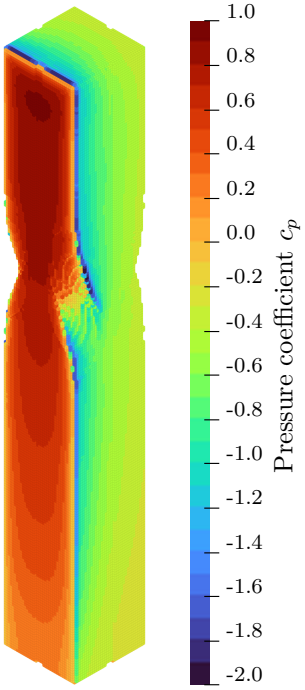

(b) Karl

Figure B.2: Distribution of pressure coefficients c_p for each typology.

C

Case study C: Expanded results

Annex C presents the results of the shape study investigation, determining whether the shape can be assumed to perform aerodynamically as a triangular prism. These results can be compared to the studies performed by Abdusemed et al. (2015), and Jendzelovsky et al., (2017).

The results are sampled at height 6 and 7 for each orientation of 0, 90 and 180 degrees.

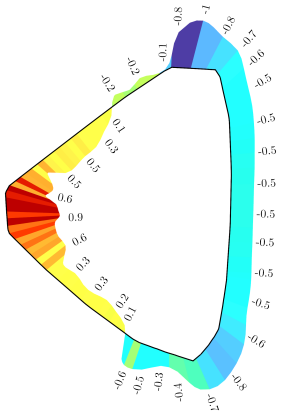

(a) z=7, 0 degree

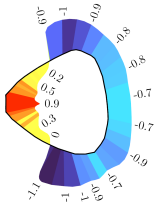

(b) z=6, 0 degree

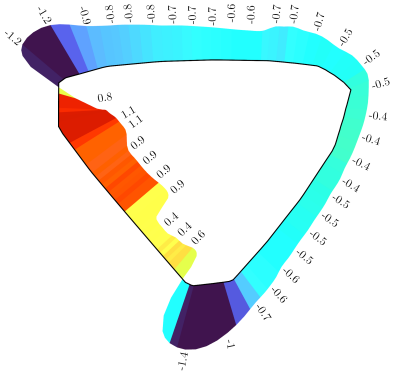

(c) z=7, 90 degree

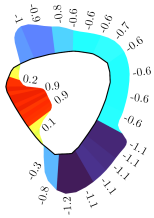

(d) z=6, 90 degree

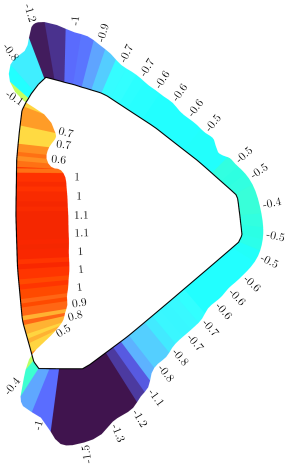

(e) z=7, 180 degree

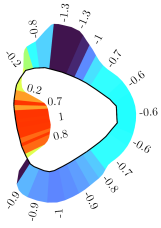

(f) z=6, 180 degree

Figure C.1: Pressure coefficients c_p of each sample location, with three different rotations.

DEPARTMENT OF ARCHITECTURE AND CIVIL ENGINEERING
DEPARTMENT OF MECHANICS AND MARITIME SCIENCES
CHALMERS UNIVERSITY OF TECHNOLOGY
Gothenburg, Sweden
www.chalmers.se

CHALMERS
UNIVERSITY OF TECHNOLOGY